FIG. 1 Accuracy curve of recurrence of B-type HCC (a) and C-type HCC (b) based on weighted voted algorithm with a leave-one-out cross validation. The 101 discriminator genes marked top accuracy (100%) in B-type HCC. The 119 discriminator genes marked top accuracy (91.7%) in C-type HCC. Accuracy = (TP + TN)/ (TP + TN + FP + FN). Expression levels of discriminator genes (top accuracy) in B-type HCC (c) and C-type HCC (d). Magenta and cyan indicate relative high and low expression levels in each sample, respectively. These discriminator genes expressed stably high in the early recurrence groups and stably low in the nonrecurrence groups

interpret the potential biological mechanisms objectively. We first applied GSEA to identify functional genetic pathways (GenMAPP database) that correlate with the entire ranked gene list of B-type HCC recurrence, sorted by the average of the correlation coefficient, "ideal discriminator method." Of the 67 gene sets, 10 contained significantly abundant genes whose products were involved in specific metabolic and signaling pathways, with nominal *P* values less than .05 (Table 2). These pathways included *Ribosomal Proteins* (*P* < .001), *Proteasome* (*P* < .001), *mRNA Processing Reactome* (*P* < .001), *Translation Factors* (*P* = .009), *RNA Transcription Reactome* (*P* = .012), *G1 to S Cell Cycle Reactome* (*P* = .014), *Calcium Regulation in Cardiac Cells* (*P* = .015), *Aminoacyl tRNA*

Biosynthesis (*P* = .016), *DNA Replication Reactome* (*P* = .019), and *Nuclear Receptors* (*P* = .039). The *FDR q* value of each of these pathways was <0.25. Likewise, we next applied GSEA for the entire ranked gene list of C-type HCC recurrence. Of the 67 gene sets, 2 contained significantly abundant genes with nominal *P* values less than .05 (Table 3). These pathways included *Ribosomal Proteins* (*P* = .003), *Pentose Phosphate Pathway* (*P* = .01). The *FDR q* value of each of the 2 pathways was also <0.25. Figure 2 shows enrichment plots of the top 2 gene sets in each type of HCC (Supplementary Tables 3 and 4 provide a list of leading edge subset genes of each *Ribosomal Proteins*. Supplementary Table 5 and 6 provide *Proteasome* and *Pentose Phosphate Pathway*, respectively. Supplementary Fig. 4 shows enrichment plots of other gene sets in B-type HCC). Notably, this result suggests that *Ribosomal Proteins* with the most significant *P* value in each analysis are associated with a common mechanism in HCC recurrence.

Correlation of the Ribosomal Pathway Alterations with Surgical Pathology

To investigate whether the activation in ribosomal pathway correlates nuclear grade (Edmondson grade) or tumor size, we performed a PCA-based classification on each 24 B-type and 60 C-type HCC patients, using the expression data of the leading-edge subset genes of ribosomal pathway (Supplementary Table 3 and 4). By this PCA classification, relatively low-activated group (cluster 1) and relatively high-activated group (cluster 2) in ribosomal pathway were identified (shown in Fig. 3a, b).

Comparing the low-activated group with the high-activated group, we tried to find any correlation between the activation in ribosomal pathway and Edmondson grade or tumor size. As a result, in B-type HCC, the activation in ribosomal pathway was related with tumor size (*P* = .03), and, in C-type HCC, the activation was related with Edmondson grade (*P* = .04) (Tables 4, 5).

DISCUSSION

Prediction of early intrahepatic recurrence and comprehension of its biological mechanism(s) are challenging problems in clinical oncology. Historically, several important studies have used the gene expression profiling to address the issue of HCC recurrence following
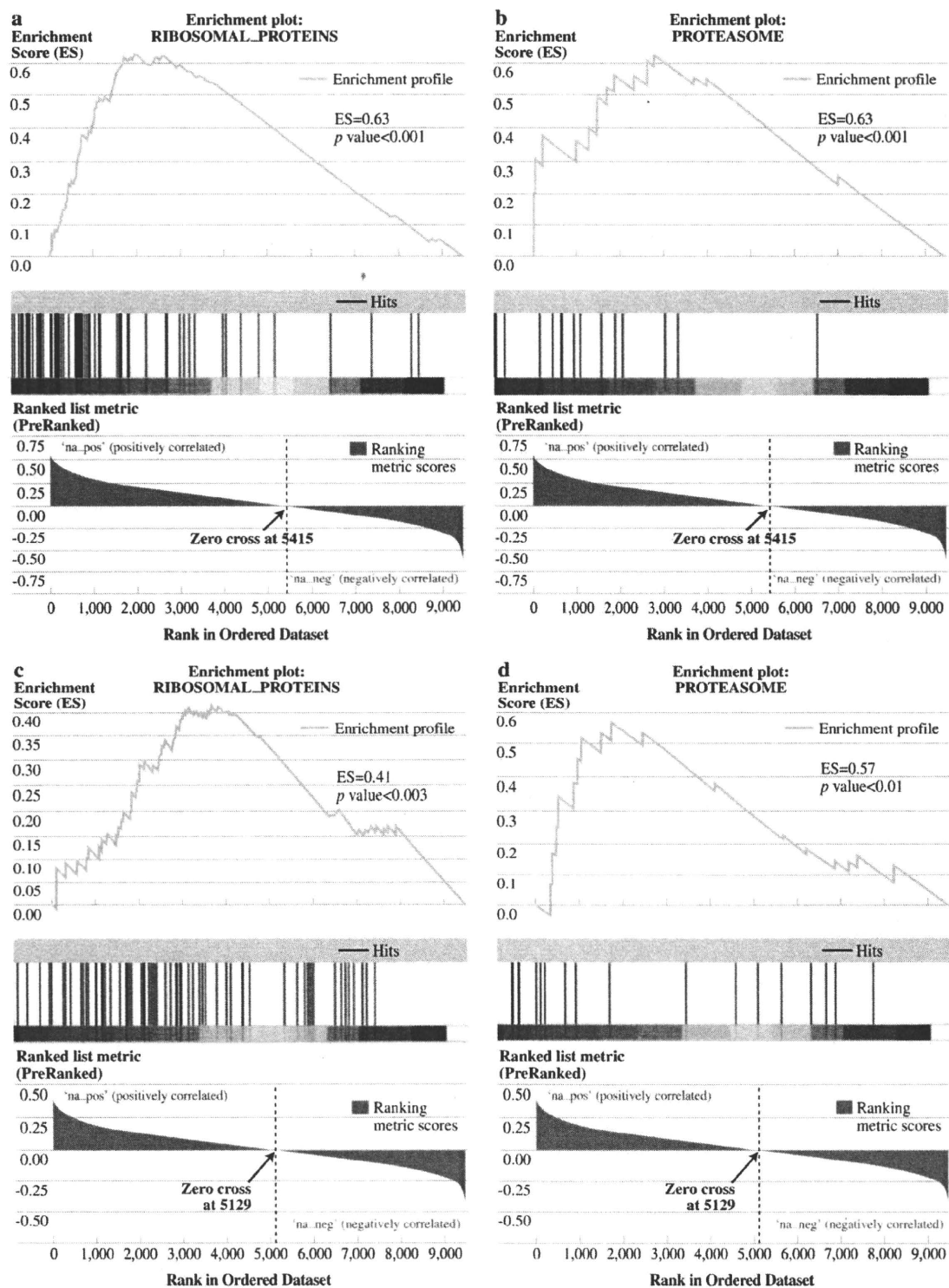
TABLE 3 Potential pathways associated with C-type HCC recurrence

Pathway name	Size	ES	NES	Nom *P* value	FDR *q* value
Ribosomal proteins	73	0.41	1.7	.003	0.12
Pentose phosphate pathway	18	0.57	1.72	.01	0.2

GSEA was performed using gene sets from GenMAPP database

ES (enrichment score) for each gene set to account for the size of the set is normalized, yielding a normalized enrichment score (NES). *NES* FDR *q* value (false discovery rate), *FDR* estimated probability that a set with a given NES represents a false positive finding; computed by comparing the tails of the observed and null distributions for the *NES*

List of the top 2 gene sets enriched in the ranked gene list of C-type HCC recurrence with nominal *P* value of <.05. The gene list is sorted in Nom *P* value ascending order

TABLE 2 Potential pathways associated with B-type HCC recurrence

Pathway name	Size	ES	NES	Nom *P* value	FDR *q* value
Ribosomal proteins	73	0.63	2.74	<.001	<0.001
Proteasome	17	0.63	1.93	<.001	0.011
mRNA processing reactome	82	0.4	1.78	<.001	0.034
Translation factors	25	0.52	1.76	.009	0.032
RNA transcription reactome	27	0.47	1.65	.012	0.059
G1 to S cell cycle reactome	44	0.41	1.62	.014	0.06
Calcium regulation in cardiac cells	87	0.33	1.5	.015	0.12
Aminoacyl tRNA biosynthesis	15	0.57	1.69	.016	0.048
DNA replication reactome	25	0.48	1.64	.019	0.057
Nuclear receptors	27	0.44	1.51	.039	0.118

GSEA was performed using gene sets from GenMAPP database

ES (enrichment score) for each gene set to account for the size of the set is normalized, yielding a normalized enrichment score (NES), *NES* FDR *q* value (false discovery rate), *FDR* estimated probability that a set with a given *NES* represents a false positive finding; computed by comparing the tails of the observed and null distributions for the *NES*

List of the top 10 gene sets enriched in the ranked gene list of B-type HCC recurrence with nominal *P* value of <.05. The gene list is sorted in Nom *P* value ascending order

FIG. 2 Enrichment plots for *Ribosomal Proteins* (**a**), *Proteasome* (**b**), *Ribosomal Proteins* (**c**), and *Pentose Phosphate Pathway* (**d**) associated with B-type (**a**) and (**b**) and C-type (**c**) and (**d**) HCC recurrences. Top, the running enrichment score for the gene set as the analysis sweeps through the entire ranked list sorted by the average of the correlation coefficient. The score at the peak of the plot is the enrichment score (ES) for the gene set. Middle, members of the gene set appear in a ranked list of genes. Bottom, the value of the ranking metric along the list of ranked genes
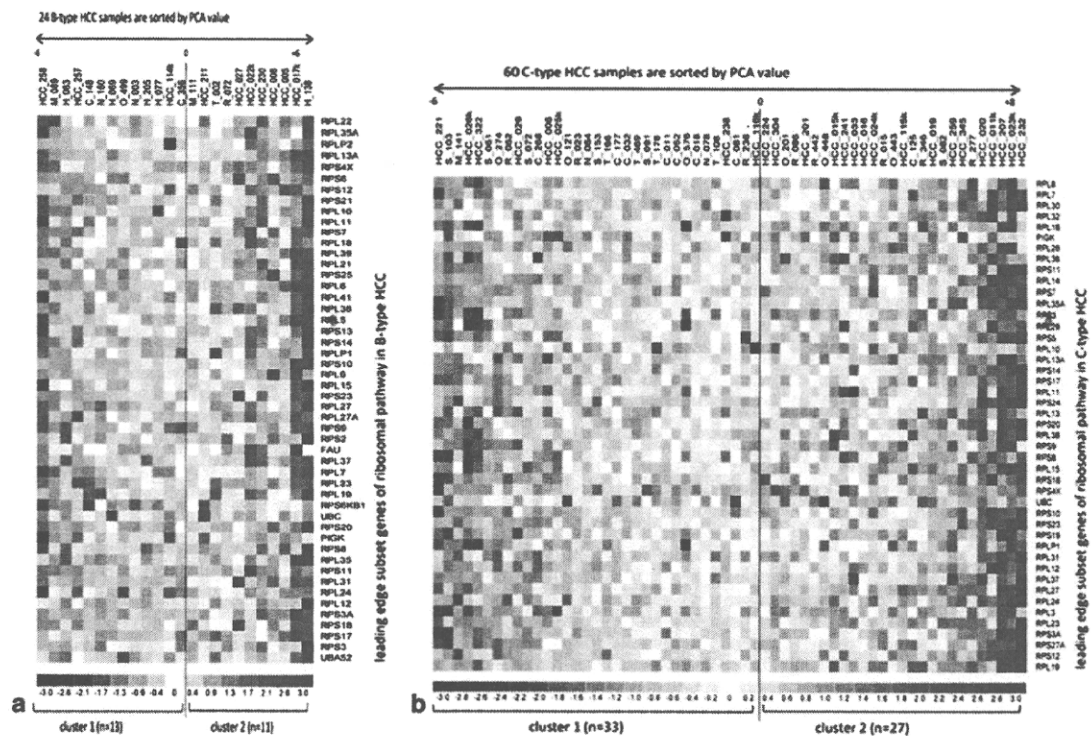
FIG. 3 PCA-based classification of patients using the expression profile of leading-edge subset genes of *Ribosomal Proteins* in B-type (a) and C-type (b) HCC recurrence. Depending on whether the value of PC1 is greater than 0 or not, patients were divided into 2 groups of low (cluster 1) or high-activated (cluster 2) in corresponding pathway

resection.[10,12] Iizuka et al. developed a system consisting of 12 genes to accurately predict early intrahepatic recurrence or nonrecurrence for patients with HCC, as an alternative to the SVM (support vector machine)-based system.[10] Yoshioka et al. defined differentially expressed 172 genes as classifier gene set using full genes based on a weighted vote (WV) algorithm with a leave-one-out cross validation.[12] Here, to understand the biological mechanisms of B-type and C-type HCC recurrences, we generated informative discriminator genes for characteristic regulator associated with each B-type and C-type HCC recurrence using "ideal discriminator method." However, selecting the discriminator genes with top accuracy did not lead to detection of common regulatory genes or different characteristic networks, because the size of the discriminator genes was so small that the statistical evaluation was prone to ascertainment bias, and the information in the discriminator genes was swamped by the number of noninformative genes. This fact suggested that comparison to discriminator genes limited by a statistical threshold might be unsuitable to reveal inherent regulatory insights related to cancer biology.

In the present study, to overcome these challenges, we applied GSEA to explore certain specific activated pathways from the entire ranked gene list, which was sorted by

TABLE 4 Comparison between ribosomal proteins low-activated group and high-activated group of *B-type HCC* in Edmonson grade and tumor size

	Cluster 1 Low-activated group ($n = 13$)	Cluster 2 High-activated group ($n = 11$)	P value
Edmondson grade			.12[a]
I, II	8	3	
III, IV	5	8	
Tumor size			.003[a]
≥5 cm	0	6	
<5 cm	13	5	

All P values are for comparison of low-activated and high-activated groups

[a] By Fisher exact probability test

the average of the correlation coefficient, "ideal discriminator method." Interestingly, it was revealed that B-type and C-type HCC have a common biological process, *Ribosomal Proteins*, associated with intrahepatic recurrence, which was not detected at the level of discriminator genes. Many *Ribosomal Proteins* take various roles that are independent of protein biosynthesis. In particular, metastatic cancer cells, which show an increase in cell-cycle

TABLE 5 Comparison between ribosomal proteins low-activated group and high-activated group of *C-type HCC* in Edmonson grade and tumor size

	Cluster 1 Low-activated group ($n = 33$)	Cluster 2 High-activated group ($n = 27$)	P value
Edmondson grade			.04[a]
I, II	27	15	
III, IV	6	12	
Tumor size			.71[a]
≥5 cm	5	3	
<5 cm	28	24	

All *P* values are for comparison of low-activated and high-activated groups

[a] By Fisher exact probability test

progression, might require more ribosomal components to sustain increased proliferation. To investigate whether the activation in ribosomal pathway correlates Edmondson grade or tumor size, we performed a PCA-based classification. These results implicate that the differences in the ribosomal pathway might be due to differences in proliferation rate.

In relation to B-type HCC, *Proteasome* was revealed as one of characteristic regulatory pathways of early intrahepatic recurrence. The *Proteasome* is a ubiquitous enzyme complex that plays a critical role in the degradation of many proteins involved in cell-cycle regulation, apoptosis, and angiogenesis. In colorectal cancer, the *Proteasome* subunit PSMA7 is differentially expressed, and overexpression of PSMA7 correlated significantly with liver metastasis, which was similar to our result (Supplementary Table 5).[24] On the other hand, in C-type HCC recurrence, we detected *Pentose Phosphate Pathway* as a specific regulatory pathway. Increased anaerobic glucose fermentation to lactate, leading to oxygen- and mitochondria-independent ATP generation, is a hallmark of aggressive cancer growth. The enzymes of the oxidative branch of the *Pentose Phosphate Pathway*, glucose-6-phosphate-dehydrogenase (G6PD) and 6-phosphogluconate dehydrogenase, are triggered by increased demand for NADPH, whereas the enzymes of the nonoxidative branch (transketolase, transaldolase) are triggered by increased demand for ribose and energy.[25] In a study of renal cell carcinoma, it was reported that transketolase and G6PD activities were extremely elevated in tumor tissues and transketolase was more elevated in metastasizing tumors.[26] Actually, our data also showed that G6PD, transketolase and transaldolase were upregulated in early intrahepatic recurrence samples of C-type HCC (Supplementary Table 6). Therefore, we speculate that progressing tumors are characterized by specific upregulation of the nonoxidative branch of the *Pentose Phosphate Pathway*,

providing sufficient supplies of ribose and energy, and supporting acidification of the tumor microenvironment, which is a major step in invasive tumor growth and metastasis.[26]

In this study, the point we emphasize is that HCC might be a heterogeneous disease characterized by a dysregulation of multiple pathways related to intrahepatic metastasis. Acting against such genomic portrait according to virus infection provides therapeutic targets for new targeted biologic therapies, which, in the future, might constitute a key for fighting cancer. A growing number of therapy options, alone or in combination with background treatments (chemotherapy, etc.), will allow oncologists a better adaptation of treatment to patients and disease characteristics, which might improve clinical efficacy.

REFERENCES

1. Parkin DM. Global cancer statistics in the year 2000. *Lancet Oncol.* 2001;2:533–43.
2. Poon RT, Fan ST, Ng IO, Lo CM, Liu CL, Wong J. Different risk factors and prognosis for early and late intrahepatic recurrence after resection of hepatocellular carcinoma. *Cancer.* 2000;89:500–7.
3. Llovet JM, Burroughs A, Bruix J. Hepatocellular carcinoma. *Lancet.* 2003;362:1907–17.
4. Thiery JP. Epithelial-mesenchymal transitions in tumour progression. *Nat Rev Cancer.* 2002;2:442–54.
5. Piccart-Gebhart MJ, Procter M, Leyland-Jones B, Goldhirsch A, Untch M, Smith I, et al. Trastuzumab after adjuvant chemotherapy in HER2-positive breast cancer. *N Engl J Med.* 2005;353:1659–72.
6. Romond EH, Perez EA, Bryant J, Suman VJ, Geyer CE, Jr., Davidson NE, et al. Trastuzumab plus adjuvant chemotherapy for operable HER2-positive breast cancer. *N Engl J Med.* 2005;353:1673–84.
7. Ramaswamy S, Ross KN, Lander ES, Golub TR. A molecular signature of metastasis in primary solid tumors. *Nat Genet.* 2003;33:49–54.
8. Armstrong SA, Staunton JE, Silverman LB, Pieters R, den Boer ML, Minden MD, et al. MLL translocations specify a distinct gene expression profile that distinguishes a unique leukemia. *Nat Genet.* 2002;30:41–7.
9. Iizuka N, Oka M, Yamada-Okabe H, Mori N, Tamesa T, Okada T, et al. Comparison of gene expression profiles between hepatitis B virus- and hepatitis C virus-infected hepatocellular carcinoma by oligonucleotide microarray data on the basis of a supervised learning method. *Cancer Res.* 2002;62:3939–44.
10. Iizuka N, Oka M, Yamada-Okabe H, Nishida M, Maeda Y, Mori N, et al. Oligonucleotide microarray for prediction of early intrahepatic recurrence of hepatocellular carcinoma after curative resection. *Lancet.* 2003;361:923–9.
11. Ye QH, Qin LX, Forgues M, He P, Kim JW, Peng AC, et al. Predicting hepatitis B virus-positive metastatic hepatocellular carcinomas using gene expression profiling and supervised machine learning. *Nat Med.* 2003;9:416–23.

12. Yoshioka S, Takemasa I, Nagano H, Kittaka N, Noda T, Wada H, et al. Molecular prediction of early recurrence after resection of hepatocellular carcinoma. *Eur J Cancer.* 2009;5:881–9.

13. Wang SM, Ooi LL, Hui KM. Identification and validation of a novel gene signature associated with the recurrence of human hepatocellular carcinoma. *Clin Cancer Res.* 2007;13:6275–83.

14. Woo HG, Park ES, Cheon JH, Kim JH, Lee JS, Park BJ, et al. Gene expression-based recurrence prediction of hepatitis B virus-related human hepatocellular carcinoma. *Clin Cancer Res.* 2008;14:2056–64.

15. Subramanian A, Tamayo P, Mootha VK, Mukherjee S, Ebert BL, Gillette MA, et al. Gene set enrichment analysis: a knowledge-based approach for interpreting genome-wide expression profiles. *Proc Natl Acad Sci USA.* 2005;102:15545–50.

16. Monti S, Savage KJ, Kutok JL, Feuerhake F, Kurtin P, Mihm M, et al. Molecular profiling of diffuse large B-cell lymphoma identifies robust subtypes including one characterized by host inflammatory response. *Blood.* 2005;105:1851–61.

17. Yang C, Zeisberg M, Lively JC, Nyberg P, Afdhal N, Kalluri R. Integrin alpha1beta1 and alpha2beta1 are the key regulators of hepatocarcinoma cell invasion across the fibrotic matrix micro-environment. *Cancer Res.* 2003;63:8312–7.

18. Takeno A, Takemasa I, Doki Y, Yamasaki M, Miyata H, Takiguchi S, et al. Integrative approach for differentially overexpressed genes in gastric cancer by combining large-scale gene expression profiling and network analysis. *Br J Cancer.* 2008;99:1307–15.

19. Kittaka N, Takemasa I, Takeda Y, Marubashi S, Nagano H, Umeshita K, et al. Molecular mapping of human hepatocellular carcinoma provides deeper biological insight from genomic data. *Eur J Cancer.* 2008;44:885–97.

20. Troyanskaya OG, Garber ME, Brown PO, Botstein D, Altman RB. Nonparametric methods for identifying differentially expressed genes in microarray data. *Bioinformatics.* 2002;18:1454–61.

21. Veer LJ, Dai H, van de Vijver MJ, He YD, Hart AA, Mao M, et al. (2002) Gene expression profiling predicts clinical outcome of breast cancer. *Nature* 415: 530–6.

22. Golub TR, Slonim DK, Tamayo P, Huard C, Gaasenbeek M, Mesirov JP, et al. Molecular classification of cancer: class discovery and class prediction by gene expression monitoring. *Science.* 1999;286:531–7.

23. Dahlquist KD, Salomonis N, Vranizan K, Lawlor SC, Conklin BR. GenMAPP, a new tool for viewing and analyzing microarray data on biological pathways. *Nat Genet.* 2002;31:19–20.

24. Hu XT, Chen W, Wang D, Shi QL, Zhang FB, Liao YQ, et al. The proteasome subunit PSMA7 located on the 20q13 amplicon is overexpressed and associated with liver metastasis in colorectal cancer. *Oncol Rep.* 2008;19:441–6.

25. Langbein S, Zerilli M, Zur Hausen A, Staiger W, Rensch-Boschert K, Lukan N, et al. Expression of transketolase TKTL1 predicts colon and urothelial cancer patient survival: Warburg effect reinterpreted. *Br J Cancer.* 2006;94:578–85.

26. Langbein S, Frederiks WM, zur Hausen A, Popa J, Lehmann J, Weiss C, et al. Metastasis is promoted by a bioenergetic switch: new targets for progressive renal cell cancer. *Int J Cancer.* 2008;122:2422–8.

CD13 is a therapeutic target in human liver cancer stem cells

Naotsugu Haraguchi,[1,2] Hideshi Ishii,[1,3] Koshi Mimori,[3] Fumiaki Tanaka,[3] Masahisa Ohkuma,[4] Ho Min Kim,[1] Hirofumi Akita,[1] Daisuke Takiuchi,[1] Hisanori Hatano,[1] Hiroaki Nagano,[1] Graham F. Barnard,[5] Yuichiro Doki,[1] and Masaki Mori[1]

[1]Department of Gastroenterological Surgery, Graduate School of Medicine, Osaka University, Osaka, Japan. [2]Excellent Young Researchers Overseas Visit Program, Japan Society for the Promotion of Science (JSPS), Tokyo, Japan. [3]Department of Surgery, Medical Institute of Bioregulation, Kyushu University, Oita, Japan. [4]Department of Surgery, Jikei University School of Medicine, Tokyo, Japan. [5]Department of Medicine, University of Massachusetts Medical School, Worcester, Massachusetts, USA.

Cancer stem cells (CSCs) are generally dormant or slowly cycling tumor cells that have the ability to reconstitute tumors. They are thought to be involved in tumor resistance to chemo/radiation therapy and tumor relapse and progression. However, neither their existence nor their identity within many cancers has been well defined. Here, we have demonstrated that CD13 is a marker for semiquiescent CSCs in human liver cancer cell lines and clinical samples and that targeting these cells might provide a way to treat this disease. CD13+ cells predominated in the G0 phase of the cell cycle and typically formed cellular clusters in cancer foci. Following treatment, these cells survived and were enriched along the fibrous capsule where liver cancers usually relapse. Mechanistically, CD13 reduced ROS-induced DNA damage after genotoxic chemo/radiation stress and protected cells from apoptosis. In mouse xenograft models, combination of a CD13 inhibitor and the genotoxic chemotherapeutic fluorouracil (5-FU) drastically reduced tumor volume compared with either agent alone. 5-FU inhibited CD90+ proliferating CSCs, some of which produce CD13+ semiquiescent CSCs, while CD13 inhibition suppressed the self-renewing and tumor-initiating ability of dormant CSCs. Therefore, combining a CD13 inhibitor with a ROS-inducing chemo/radiation therapy may improve the treatment of liver cancer.

Introduction

Functional and morphologic heterogeneity exists in a tumor with a hierarchy in which tumor growth is driven by a small subset of cancer stem cells (CSCs) (1). Like normal tissue stem cells, which are capable of self renewal and multidifferentiation, CSCs have the ability to reconstitute tumors (2). In the hematologic cell lineage, stem cells exist in the dormant phase and can be detected as a side population (SP) (3). Generally, CSCs, like somatic tissue stem cells, proliferate slowly, i.e., they are in the dormant or slow-growing phase of the cell cycle. This partially accounts for their therapeutic refractoriness to chemo/radiation therapy, tumor relapse, and presumably metastasis. The CSCs of acute myeloid leukemia (4) and chronic myeloid leukemia (5) also survive in the dormant G_0 phase of the cell cycle in a bone marrow niche after chemotherapy. Relapses and metastases of breast cancer often occur after intervals of several decades, suggesting the involvement of a deep dormant phase for CSCs (6). The majority of liver cancers are superimposed on a background of chronic hepatitis and hepatic cirrhosis. Therefore, it may be difficult to distinguish between intrahepatic metastasis through portal or hepatic venules and metachronous multicentric development of liver cancer in a precancerous background. However, there are some cases of liver cancer in which cancer recurs in the liver or metastasizes to the lung and bone several years after radical hepatectomy or liver transplantation. This suggests that some slow-growing cancer cells also exist in liver cancer but these may not be in deep dormancy like breast cancer CSCs.

Anticancer reagents in clinical use generally affect division and proliferation of cancer cells. This could result in elimination of proliferating cancer cells but not reduce the survival of CSCs in the dormant or slow-growing phase. Thus, the identification and characterization of dormant or slow-growing CSCs are important for developing novel therapeutic approaches.

In studies of hepatocellular carcinoma (HCC) (7), the fifth most common cancer in the world, the SP fraction (8), CD133+ (9–11), CD44+ (11, 12), CD90+ (12, 13), and epithelial cell adhesion molecules (14) were reported as markers of CSCs or cancer-/tumor-initiating cells. The majority of CSC studies focus on identification of cell markers to enrich cell populations that have high tumor initiation ability in immune-deficient mice. In the field of liver cancer CSCs, there have been few reports describing dormant or slow-growing CSCs that include their cellular characteristics or indicate a way to target these cells based on cytological evidence. In addition, there have been few reports that clearly indicate the interrelationships among these candidate markers.

In a previous study (similar to hematopoietic and leukemic studies), we reported that the SP fraction enriches the CSC-like fractions. Cells of the SP fraction express both hepatocyte and cholangiocyte markers, show high resistance to anti-cancer agents, and high tumorigenicity in NOD/SCID mice (8). Based on our previous data (8) and applying the techniques of hematopoietic stem cell studies (3–5), our aims were as follows: first, to clarify the relationships between reported candidate CSC markers; second, to assess whether dormant CSCs exist in liver cancer and to concentrate on cell-surface markers, which definitively identify potentially dormant CSCs; third, to clarify the cellular characteristics of potentially dormant CSCs and to identify the mechanisms that protect potentially dormant CSCs from chemo/radiation therapy; finally, to identify target molecules of liver cancer CSCs to initiate novel approaches that could lead to a future radical cure for liver cancer.
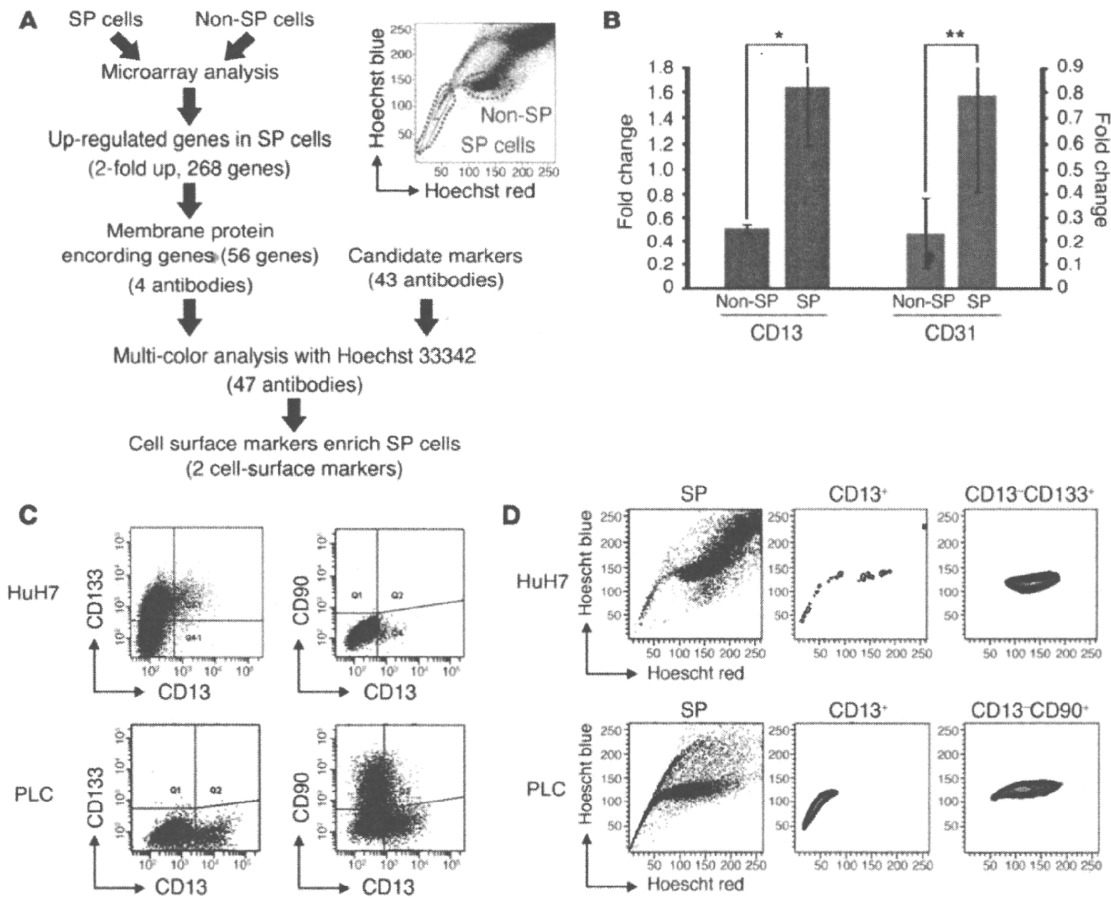
Figure 1
CD13 is a candidate marker of the SP fraction. (**A**) The strategy used to identify cell-surface markers closely related to the SP fraction. We determined CD13 and CD31 as candidate markers for identifying SP cells. (**B**) Both CD13 and CD31 expression in HuH7 cells were compared in SP and non-SP cells by semiquantitative RT-PCR. Data represent mean ± SD from independent experiments of fractions differentially sorted by flow cytometry. *$P < 0.01$; **$P = 0.076$ versus non-SP fractions. The cut-off lines were determined using isotype controls. (**C**) Expression of CD13, CD133, and CD90 in HuH7 (upper panels) and PLC/PRF/5 cells (lower panels). Horizontal and vertical axes denote expression intensity. (**D**) The SP fraction is recognized as a "beak" appearing beside the G_1 phase fraction. The relationship between CD13+ and CD13– cells and the SP fraction was studied using multicolor flow cytometry.

Results

CD13 is a candidate marker closely correlated with SP cells. To identify specific cell-surface markers that correlate with the SP fraction, we utilized our previous data sets of SP and non-SP fraction gene expression profiles obtained using microarray analyses (8). From a list of 268 genes upregulated in the SP cells (with a fold change > 2) (8), we selected 56 genes that potentially encode cell-surface proteins via the UniProtKB database (http://www.uniprot.org/). Working from the list of 56 upregulated genes (Supplemental Table 1; supplemental material available online with this article; doi:10.1172/JCI42550DS1) and an additional 43 markers reported to be closely associated with normal stem cells and CSCs, we tested 47 commercially available antibodies (Supplemental Table 2) to identify surface markers that were enriched in the SP fraction (Figure 1A).

During this screening, we identified 2 candidate markers, CD13 and CD31. The expression analysis of CD13 was 1.64 ± 0.45 in the SP and 0.51 ± 0.03 in the non-SP cell fraction ($P < 0.01$) (Figure 1B). We focused on CD13 in the current study, since the expres-

sion of CD31 was abundant in the $G_2/M/SP$ fraction but was not universal in the liver cancer cell lines studied by us (HuH7, PLC/PRF/5, and Hep3B), and the statistical significance was weak ($P = 0.076$) (Figure 1B and Supplemental Figure 1, A and B).

Expression of CD13, CD133, and CD90 was assessed in hepatitis infection–negative (HuH7) and –positive (PLC/PRF/5) cell lines. The expression of CD133 was detected in HuH7 but not in PLC/PRF/5, and the expression of CD90 was detected in PLC/PRF/5 but not in HuH7. The expression of CD13 was observed in both these cell lines as well as in Hep3B (Figure 1C and Supplemental Figure 1A). In HuH7 in particular, the CD13+ cells typically existed in a CD133^{strong} fraction (CD13+CD133+).

Multicolor analysis with Hoechst staining exhibited clear localization of CD13+ cells in the SP fraction of HuH7 and PLC/PRF/5, whereas the CD13–CD133+ and CD90+ fractions were localized to the G_1-to-G_2 fraction and not the SP fraction (Figure 1D). To confirm the cell-cycle status of the CD13+ cells in PLC/PRF/5, cell-cycle analysis by combined multicolor analysis and 7-amino-actinomy-
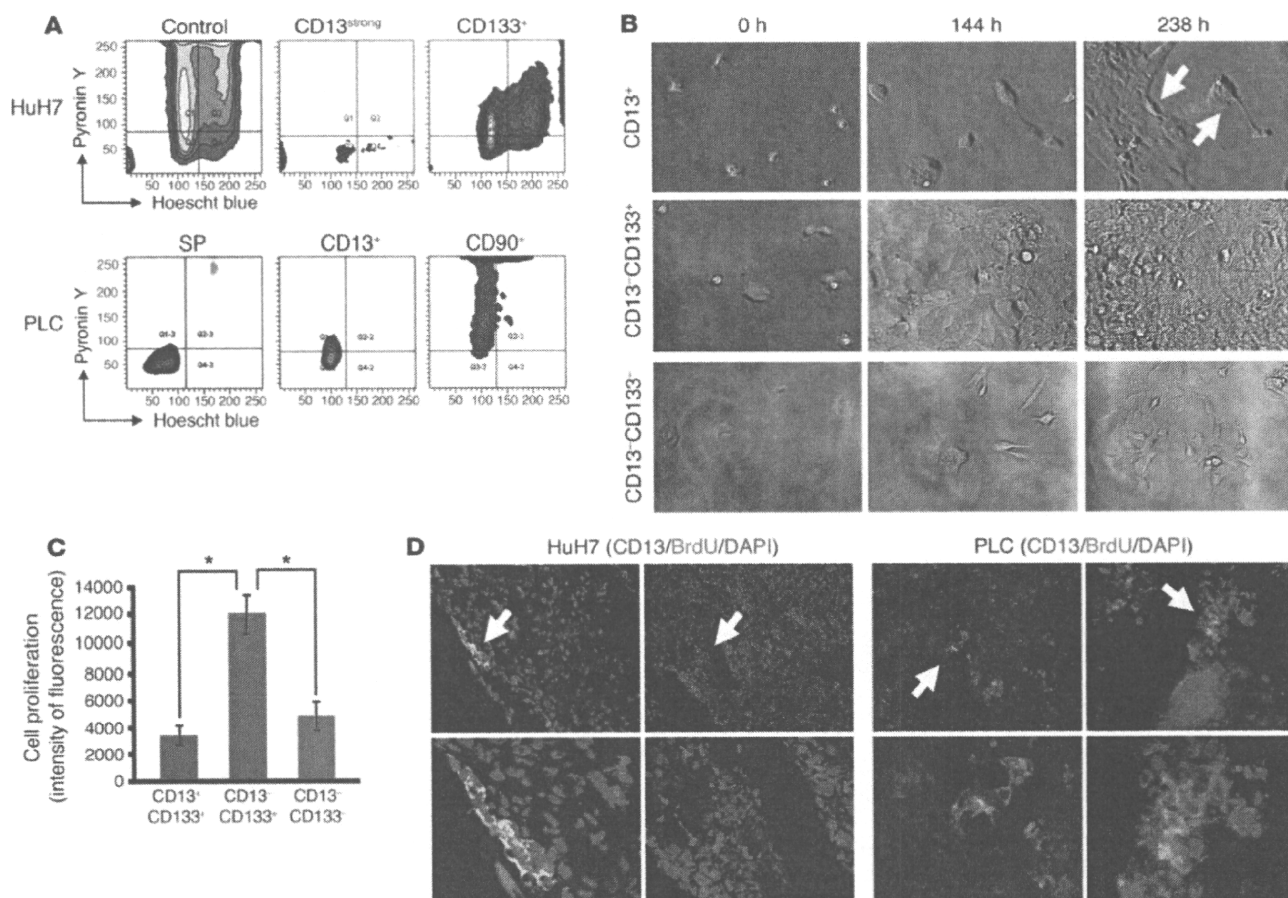
Figure 2
CD13 is a candidate marker of dormant to slow-growing CSCs. (**A**) Dormant cells can be identified using the DNA-binding dye Hoechst 33342 and RNA-binding dye PY. Dormant cells contain lower RNA levels than G_1 phase cells. Combination analysis of the cell cycle with cell-surface markers CD13, CD133, and CD90 was performed with reserpine. The cut-off lines were determined using isotype controls. (**B**) Time-lapse cell-fate tracing of HuH7 cells. Cells were labeled with PKH26GL, isolated to their CD13+, CD13−CD133+, and CD13−CD133− fractions, and traced for 238 hours. The dye-retaining cells can be identified as red-labeled cells (white arrow). Original magnification, ×20. (**C**) Proliferation assay of the CD13+CD133+, CD13−CD133+, and CD13−CD133− fractions. Data represent mean ± SD from independent experiments of fractions differentially sorted by flow cytometry. *$P < 0.05$. (**D**) BrdU-retaining cells in serially transplanted control tumor specimens of HuH7 (6 weeks after BrdU injection) and PLC/PRF/5 (10 weeks after BrdU injection). The sections were stained with anti-CD13 (red), BrdU (green), and DAPI (blue). Top panels show lower magnification of the sections of HuH7 and PLC/PRF/5 (×10, HuH7 and left panel of PLC; ×20, right panel of PLC). The lower panels show high magnification (×40) of the place indicated by white arrows in the top panels.

cin D (7-AAD) DNA labeling was performed. The CD13+CD90− population was mainly in the G_0/G_1 phase, and the CD13+CD90+ population was clearly in the S to G_2/M phase. The CD13−CD90+ cells were present in all phases of the cell cycle but were more clearly present in the G_2/M and S phases when compared with the CD13−CD90− population (Supplemental Figure 1C).

In these studies, we confirmed CD13 as a universal candidate marker that correlates with the liver cancer SP fraction. There were no definitive single markers that showed a stronger correlation to the SP fraction than CD13 and, to a lesser extent, CD31.

CD13 is a marker of tumor-initiating and potentially dormant HCC cells. Given that hematopoietic and leukemic stem cells are in the G_0 phase, identification and characterization of dormant or slow-growing cancer cell populations is very important because of these populations' relevance to chemo resistance and recurrence. Studies of CD13 expression in HuH7 and PLC/PRF/5 and their

relationships with the cell-cycle phase, using the DNA-binding dye Hoechst 33342 and the RNA-binding dye pyronin Y (PY) (3), indicated that most of the CD13+ fraction exists in the G_1/G_0 phase and the CD13strong population was clearly localized in G_0. The CD133+ population in HuH7 and the CD90+ fraction in PLC/PRF/5 were distributed in the G_1/G_0 and G_2/M phases, respectively. The relationships between the SP fraction and the G_0 cell-cycle phase were also confirmed, and the SP fraction was clearly localized in the G_0 phase under reserpine-free (ABC transporter blocker) conditions (Figure 2A).

To study the cell fate and dye-retaining capacity of HuH7 CD13+ cells, the cell-surface membrane was labeled with PKH26GL reagent and cell fate was traced for 238 hours. Equal numbers of cells were seeded for each population. The CD13+CD133+ fraction exhibited very slow growth compared with the CD13−CD133+ fraction, with the doubling time of the CD13+CD133+ fraction estimated

Table 1
Limiting dilution and serial transplantation assay of HuH7 and PLC/PRF/5 cells

Cell type	Assay	Marker/cells	1×10^2	5×10^2	1×10^3	5×10^3	1×10^4
HuH7	Limiting dilution	CD13⁺CD133⁺	2/4	2/4	3/4	3/4	–
HuH7	Limiting dilution	CD13⁻CD133⁺	0/4	0/4	3/4	4/4	–
HuH7	Limiting dilution	CD13⁻CD133⁻	0/4	0/4	0/4	0/4	–
HuH7	Serial transplantation	CD13⁺CD133⁺	0/4	1/4	3/4	4/4	3/4
HuH7	Serial transplantation	CD13⁻CD133⁺	0/4	0/4	0/4	0/4	1/4
HuH7	Serial transplantation	Control	0/4	0/6	0/6	0/6	2/6
PLC	Limiting dilution	CD13⁺CD90⁻	2/4	2/2	4/4	3/3	–
PLC	Limiting dilution	CD13⁻CD90⁺	0/4	2/2	4/4	3/3	–
PLC	Limiting dilution	CD13⁻CD90⁻	0/4	0/4	0/3	0/4	–
PLC	Serial transplantation	CD13⁺CD90⁻	0/4	2/4	3/4	3/4	3/4
PLC	Serial transplantation	CD13⁻CD90⁺	0/4	0/4	0/4	0/4	1/4
PLC	Serial transplantation	Control	0/6	0/6	0/6	1/6	2/6

at approximately 160 hours. Dye-retaining cells could be observed 238 hours after cell seeding only in the CD13⁺CD133⁺ fraction (Figure 2B and Supplemental Videos 1–3). The CD13⁻CD133⁻ fraction exhibited cell fragmentation and apoptotic changes during cell culture. To confirm CD13 expression in association with cell growth, we performed cell proliferation assays. Data from isolated HuH7 populations showed that CD13⁺CD133⁺ cells exhibited slow cell growth compared with CD13⁻CD133⁺ cells 72 hours after seeding (Figure 2C). The CD13⁻CD133⁻ population also grew slowly but maintained viability for a week, with difficulty, because of apoptosis.

Next, tumor-formation ability of each fraction was studied in HuH7 and PLC/PRF/5 cells. Limiting dilution analysis of HuH7 cells revealed that the CD13⁺CD133⁺ fraction formed tumors from 100 cells (2/4), the CD13⁻CD133⁺ fraction formed tumors from 1,000 cells (3/4), and the CD13⁻CD133⁻ fraction formed no tumors from 5,000 cells (0/4) in NOD/SCID mice after 4 weeks of observation. In PLC/PRF/5 cells, the CD13⁺CD90⁻ fraction formed tumors from 100 cells (2/4), and the CD13⁻CD90⁺ fraction formed tumors from 5,000 cells (2/2), whereas the CD13⁻CD90⁻ cells formed no tumors from 5,000 cells (0/4) in NOD/SCID mice after 6 weeks of observation (Table 1). To assess the tumor formation ability definitively, formed tumors were digested, and isolated CD13⁺CD133⁺ and CD13⁻CD133⁺ fractions of HuH7 and isolated CD13⁺CD90⁻ and CD13⁻CD90⁺ fractions of PLC/PRF/5 were serially transplanted to secondary NOD/SCID mice. As controls, nonisolated cell fractions of HuH7 and PLC/PRF/5 were also serially transplanted. Tumor formation ability of CD13⁺ cells compared with that of CD13⁻ cells in serial transplantation assay was demonstrated more clearly than that of limiting dilution assay. In HuH7, after 6 weeks of observation, the CD13⁺CD133⁺ fraction formed tumors from 500 cells (1/4), whereas the CD13⁻CD133⁺ fraction and control formed very small tumors only in 10,000 cells (1/4 in the CD13⁻CD133⁺ fraction, and 2/6 in control). In PLC/PRF/5, after 6 weeks of observation, the CD13⁺CD90⁻ formed tumors from 500 cells (2/4), and the control formed tumors from 5,000 cells (1/6), whereas the CD13⁻CD90⁺ fraction formed 1 very small tumor only in 10,000 cells (1/4) (Table 1).

To assess semiquiescent status of CD13⁺ cells in vivo, BrdU-retaining status was studied. Tumors obtained from NOD/SCID mice xenografted with HuH7 and PLC/PRF/5 cells were digested

to single cells and serially transplanted without isolation of cell-surface markers. BrdU was injected intraperitoneally. After 6 weeks for HuH7, and after 10 weeks for PLC/PRF/5, tumors were enucleated and sections were stained with anti-BrdU and anti-CD13 antibody. In the tumors derived from HuH7 cells, very small numbers of BrdU-retaining cells that also expressed CD13 were observed typically in the edge of tumor foci. BrdU-retaining cells were not observed in the tumor center. Tumors derived from PLC/PRF/5 cells grew more slowly than did those derived from HuH7 cells. BrdU-retaining cells could be identified and did express CD13. Interestingly, clusters of CD13⁺BrdU⁻ cells were observed close to CD13⁺BrdU⁺ cells, suggesting that they might be derived from the CD13⁺BrdU⁺ cells (Figure 2D).

HCC-CD13⁺ cells form spheres and produce the CD90⁺ phenotype. Sphere formation is a common characteristic of stem cells. To evaluate CD13 as a candidate CSC marker, the expression of CD13 in spheres derived from HuH7, PLC/PRF/5, and clinical HCC was studied. The expression of CD13 was increased in both HuH7 (2.0% in control vs. 67.0% in spheres; 33.5-fold increase) and PLC/PRF/5 (15.2% in control vs. 83.8% in spheres; 5.51-fold increase) (Figure 3A). There was no significant change in CD133 expression in HuH7. In PLC/PRF/5, expression of CD90 was decreased in the spheres (35.7% in control vs. 2.5% in spheres; 14.28-fold decrease). The expression of CD13 compared with that of CD133 and CD90 appeared to be associated with a more immature stem-like and dormant population. Spheres established from clinical HCC samples localized in the CD13⁺CD90⁻CD133⁻ fraction in a manner similar to that observed in PLC/PRF/5 (Figure 3B).

The time-course changes in the expression of CD13 and CD90 in PLC/PRF/5 were studied. Isolation and culture of the CD13⁺CD90⁻ fraction from the PLC/PRF/5 spheres in serum-containing media resulted in the production of CD13⁺CD90⁺ fraction after 96 hours (Figure 3C). The isolated CD13⁻CD90⁻ fraction elicited cell death within a few days and could not be maintained. Interestingly, the isolated CD13⁻CD90⁺ fraction rapidly produced the CD13⁺CD90⁻ fraction within 24 hours (Figure 3C). These findings suggest that potentially dormant CD13⁺ cells produce proliferating CD90⁺ cells and that some parts of the proliferating CD90⁺ cells also produce CD13⁺ cells. It is important to determine how this CD13⁺ population (slow-growing potentially dormant) could be maintained in a cancer cell line in vitro. Dormant or slow-growing cell populations may disappear during continuous subculturing. These findings may replicate the rapid change from dormant to active status in cancer stem-like cells, as revealed by their cell-surface markers, or the dormant cells might mimic a certain multipotent condition in cellular differentiation.

CD13⁺ cells resist chemotherapy, and CD13 inhibition drives cells to apoptosis. The change of cell-surface marker expression before and after doxorubicin (DXR) hydrochloride treatment or 5-fluorouracil (5-FU) was studied in HuH7 and PLC/PRF/5. In HuH7, CD13

A

B

C
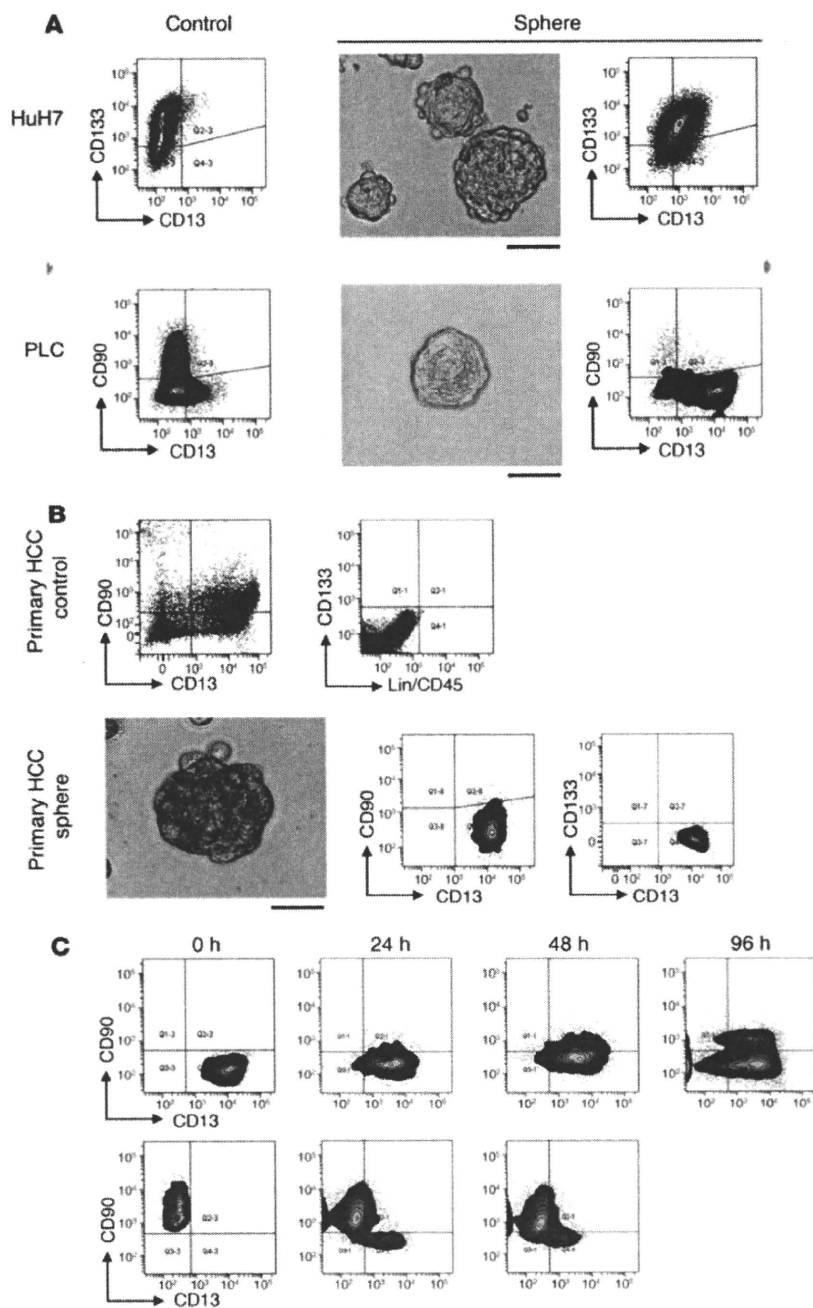
Figure 3
CD13+ cells exist as a core in HCC spheres and produce CD90+ cells. (**A**) Spheres established from HuH7 and PLC/PRF/5 cells were dissociated to single cells and the marker expressions were compared with control cells. Scale bars: 200 μm. (**B**) Expression analysis of primary human HCC cells (control) and spheres established from original human HCC cells (sphere). Scale bar: 200 μm. (**C**) The time-course expression analyses of sorted CD13+CD90− cells (upper panels) and CD13−CD90+ cells (lower panels) from PLC/PRF/5. The cut-off lines were determined using isotype controls.

assay in HuH7. The CD13+CD133+ fraction was highly resistant to DXR compared with the CD13−CD133+ and CD13−CD133− fractions, indicating consistent changes in the markers following DXR treatment (Supplemental Figure 2A). Although the CD13−CD133− fraction exhibited slow cell growth in the proliferation and cell fate study (Figure 2, B and C), this fraction showed high chemosensitivity.
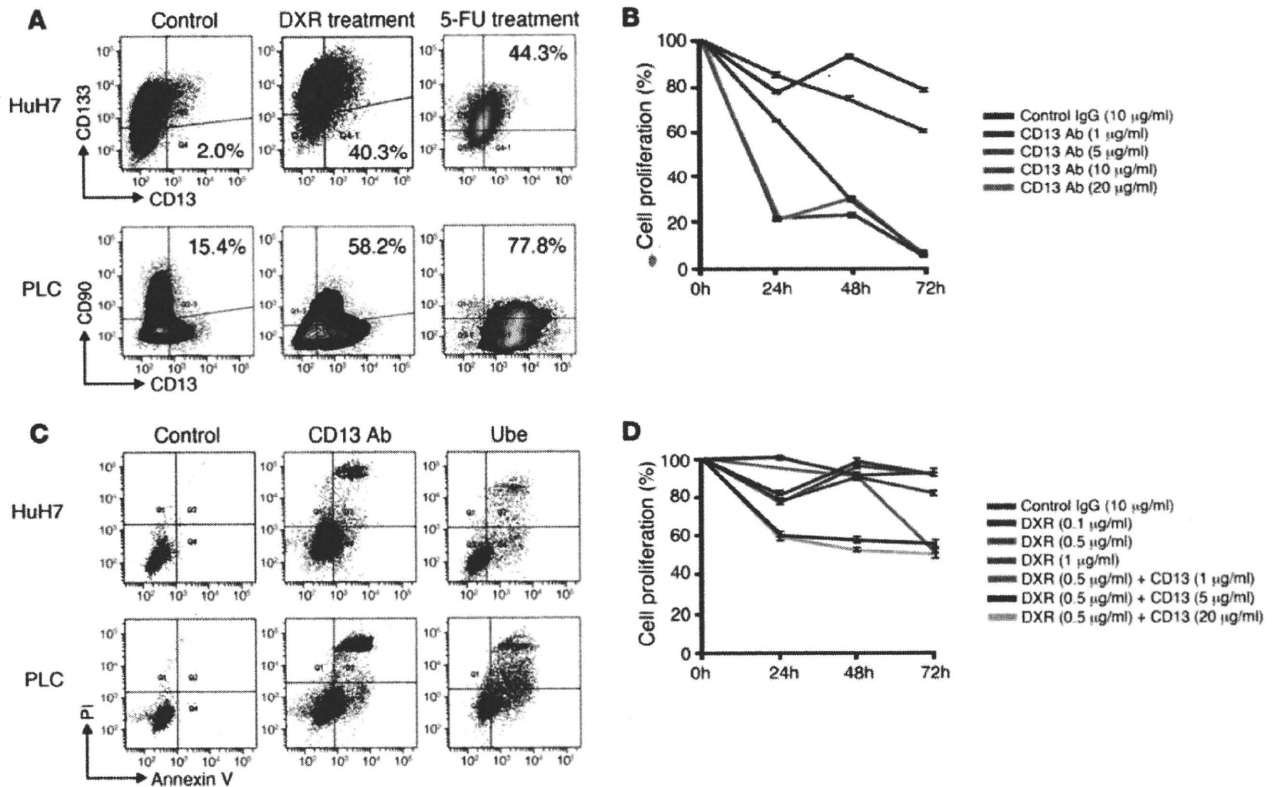
Next, the effect of CD13 inhibition on cell proliferation in HuH7 was assessed. Cell proliferation was suppressed in a concentration-dependent manner after 72 hours exposure to the CD13-neutralizing antibody. At 10 and 20 μg/ml concentrations of the CD13-neutralizing antibody, cell proliferation was suppressed by approximately 80% at 24 hours and 95% at 72 hours (Figure 4B). The apoptosis assay showed that both the CD13-neutralizing antibody and CD13 inhibitor ubenimex induced apoptosis in both HuH7 and PLC/PRF/5 after 24 hours (Figure 4C). The CD13 antibody (clone WM15) has been shown to be specific to humans and to function as a neutralizing antibody (15). Reportedly, ubenimex (bestatin) specifically blocks CD13, which antagonizes the zinc-binding site of the aminopeptidase N domain (16–19). Ubenimex is used as a therapeutic agent for adult acute nonlymphatic leukemia (20).

We then hypothesized that not only the ABC transporter (21, 22) but also CD13 is involved in cell protection against exposure to anticancer agents. DXR is a well-known ABC-trans-porter–dependent anticancer drug. We have established a DXR-resistant HuH7 clone in which 90% of cells survive in 0.5 μg/ml of DXR, whereas about 99% of parent HuH7 cells die at that concentration (Supplemental Figure 2, B and C). Inhibition of CD13 indicated approximately 50% suppression of cell proliferation in this clone (Figure 4D), and this finding suggests that CD13 inhibition can potentially suppress cells that may have multidrug-resistance capacities and remain viable after conventional anticancer drug treatments.

CD13 is expressed preferentially in therapy-resistant HCC cells. To identify the expression of CD13 in clinical HCC, HCC samples were digested and hematopoietic Lin−CD45− fractions were further

expression was increased over 20-fold by DXR or 5-FU treatment compared with control (CD13+CD133+ population in control, 2.0%; by DXR treatment, 40.3%; by 5-FU treatment, 44.3%), although expression of CD133 remained unchanged (87.1% in control vs. 88.0% after DXR treatment, 88.7% after 5-FU treatment). In PLC/PRF/5, after treatment with DXR, the CD13+CD90− fraction was also increased and the CD13−CD90+ fraction was shifted to the CD13 positive (the CD13+CD90− fraction of control was 15.4% and of DXR treatment was 58.2%). After treatment with 5-FU, the remaining cells were more clearly localized in the CD13+CD90− fraction (77.8%) (Figure 4A). The chemo-resistance ability of the CD13+ cells was also confirmed by cell proliferation
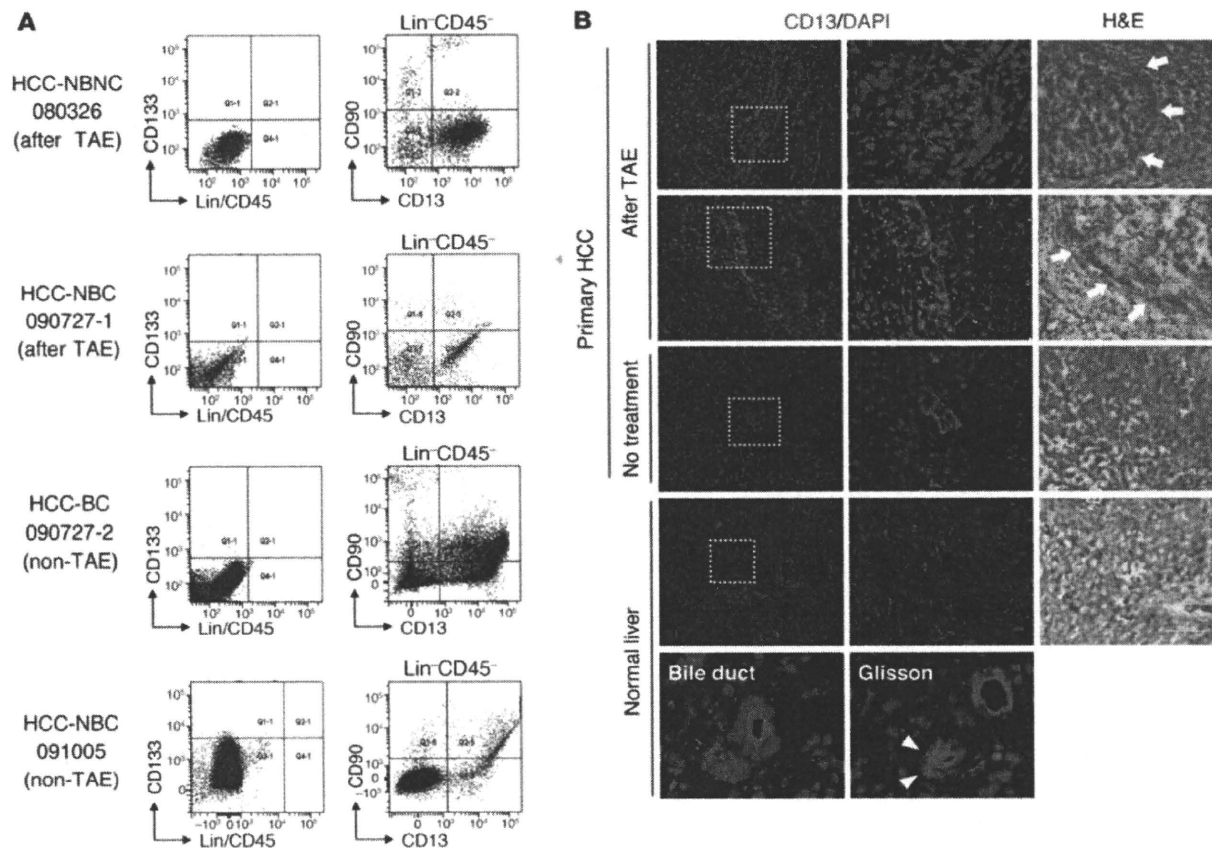
Figure 4
CD13+ cells resist chemotherapy, and inhibition of CD13 elicits cellular apoptosis. (A) The HuH7 and PLC/PRF/5 cells were treated with 0.1 μg/ml of DXR or 1 μg/ml of 5-FU for 72 hours. The changes in cell-surface markers were compared with controls. The percentages of CD13+CD133+ in HuH7 and CD13+CD90− populations in PLC/PRF/5 are shown in figure. (B) Effect of CD13 inhibition on cell proliferation. HuH7 cells were treated with various concentrations of anti-human mouse IgG₁ CD13-neutralizing antibody. As a negative control, 10 μg/ml of anti-human mouse IgG₁ antibody was used. (C) Inhibition of CD13 induces cell apoptosis. Cells were treated with 1–20 μg/ml of CD13-neutralizing antibody or 50–500 μg/ml of ubenimex for 24 hours. Data show each case of 5 μg/ml of CD13-neutralizing antibody and 100 μg/ml of ubenimex treatment. (D) The effect of CD13-neutralizing antibody on DXR-R HuH7. The DXR-R clone was established with continuous treatment in 1 μg/ml of DXR and a selection of viable colonies. In 0.5 μg/ml of DXR, most control HuH7 cells die after 72 hours, whereas over 90% of DXR-R cells survive. The DXR-R HuH7 cells were cultured with 1–20 μg/ml of CD13-neutralizing antibody for 72 hours. Control, treated with 10 μg/ml of anti-human mouse IgG₁ antibody.

analyzed by multicolor flow cytometry. In all 12 clinical HCC samples, including 3 cases of non–hepatitis-derived HCC (1 case recurred after transcatheter arterial embolization [TAE]) and 9 cases of hepatitis-derived HCC (4 cases recurred after TAE), no CD133 expression was observed. In all cases, CD13 and CD90 expression was observed in the following 4 subpopulations: CD13+CD90+, CD13+CD90−, CD13−CD90+, and CD13−CD90−. In cases that recurred after TAE, the CD13+CD90− fraction was more abundant than that in non-TAE cases (48% ± 12% in TAE cases vs. 8% ± 4% in non-TAE cases; 6-fold increase), whereas the CD13−CD90+ fraction was more abundant in non-TAE cases than in TAE cases (40% ± 18% in non-TAE cases vs. 12% ± 5% in TAE cases; 3.3-fold increase) (Figure 5A). In all 12 clinical HCC samples, the expression patterns were very similar to that of PLC/RLF/5, indicating its usefulness as an HCC model. Of course, the percentages of cells just indicate the percentage that survived after mechanical and enzymatic digestion. The majorities of HCC cells retain the cellular functions of liver cells, accumulate fat and glycogen, and produce bilirubin. Also, they are relatively

bigger than other kinds of cancer cells and may be more easily damaged by mechanical and enzymatic digestion.

The expression of CD13 was confirmed in fresh frozen surgical specimens. The CD13+ HCC cells typically existed along the fibrous capsule forming cellular clusters after TAE. In non-TAE cases, the CD13+ HCC cells usually formed small cellular clusters inside the cancer foci (Figure 5B). CD13 was expressed on the cell surface in HCC cases. In normal liver samples, CD13 was expressed in the sinusoid with a linear staining pattern and in bile ducts with an intraductal pattern; this was different in the HCC samples. The immunohistochemical findings for the post-TAE cases support clinical experience because HCC recurrence after TAE usually occurs at the fibrous capsule and chemoresistant viable HCC cells exist mainly around the fibrous capsule.

Interestingly, some small canalicular structures near the bile ducts expressed CD13 on the cell surface, and these are suggested to be liver stem/progenitor cells, since it has been reported that normal liver stem/progenitor cells express CD13 (23). In our studies, spheres established from the normal liver were predominantly

Figure 5
CD13 expression in clinical HCC samples with or without TAE. (**A**) Expression analysis of clinical HCC samples. The nonhematopoietic Lin/CD45- fraction was analyzed. The data show 2 typical TAE and non-TAE cases, nonhepatitis virus infection (NBNC; first row), nonhepatitis B but hepatitis C infection (NBC; second row), both hepatitis B and C infection (BC; third row), and another nonhepatitis B but hepatitis C infection (fourth row). The cut-off lines were determined using isotype controls. (**B**) Immunohistochemical analysis of HCC and normal liver samples stained with anti-human CD13 (red) and DAPI (blue) for the nucleus. Each middle panel shows a high magnification (×40) of the white dotted square in each left-hand column (×10). The right columns exhibit H&E stains (×10) of each adjacent frozen section. 3 typical samples from 6 HCC samples are represented. The white arrow indicates the fibrous capsule (Fc) in HCC samples, and tumor cells exist inside Fc. The upper 2 samples show HCC after TAE, and the middle samples are from no-TAE cases. In HCC samples, CD13 is expressed on the cell surface. The lower panels show immunohistochemical stains of normal liver obtained from surgical sections of colon cancer metastasis. Expression of CD13 in hepatic lobules is linear along the sinusoid. In the bile ducts, CD13 is expressed in an intraductal manner (lower left; bile duct, ×40). In some small canalicula present near the bile duct, CD13 is expressed on the cell surface (lower right; Glisson, ×40).

CD13$^+$CD90$^+$CD133$^+$, with a multidifferentiation potential in both hepatocyte and cholangiocyte lineages (Supplemental Figure 3).

To assess whether the area of the fibrous capsule contributed to the maintenance of semiquiescent CD13$^+$ cells, we stained fresh frozen tissues obtained from HCC parents with a hypoxia marker, carbonic anhydrase 9 (CA9) (24). In hematopoietic stem cells, hypoxia is well known as a hypoxic niche that plays important roles in maintaining stem cells in a dormant phase (25, 26). In the TAE samples, expression of CA9 was localized along the fibrous capsule and coexpressed CD13. In the non-TAE samples, CA9$^+$ cells formed cellular clusters in cancer foci and coexpressed CD13. In normal livers, CA9 expression was limited to the cell surface of bile ducts (Supplemental Figure 4).

CD13 inhibition elicits tumor regression. For preliminary studies, HuH7 cells were transplanted into NOD/SCID mice and treated with 5-FU to determine whether the CD13$^+$ fraction was enriched

by treatment with a DNA synthesis inhibitor or not. We used 5-FU, the most common anticancer drug in HCC treatment, to simulate the clinical setting. After 3 days of intraperitoneal administration of 5-FU (30 mg/kg), most Ki67$^+$ active cells were disrupted and remained only at small foci, and tumors were replaced by a majority of CD13$^+$Ki67$^-$ cells. In the controls, CD13 expression was limited to a small fraction with cellular clustering, and most cells expressing CD13 were Ki67$^-$. Conversely, in ubenimex-treated mice (20 mg/kg, 3 days), most of the CD13$^+$ cells were disrupted and replaced with Ki67$^+$ active cells (Figure 6A).

PLC/PRF/5 was then used for further analyses. The expression of markers in this cell line is similar to that in clinical HCC, and thus, the PLC/PRF/5 cell line is potentially useful as an HCC model. In control mice, CD13 expression was limited to a small fraction and most of the cells expressed CD90. After treatment with 5-FU (30 mg/kg, 5 days of injection and 2 days of withdrawal, 2 courses),
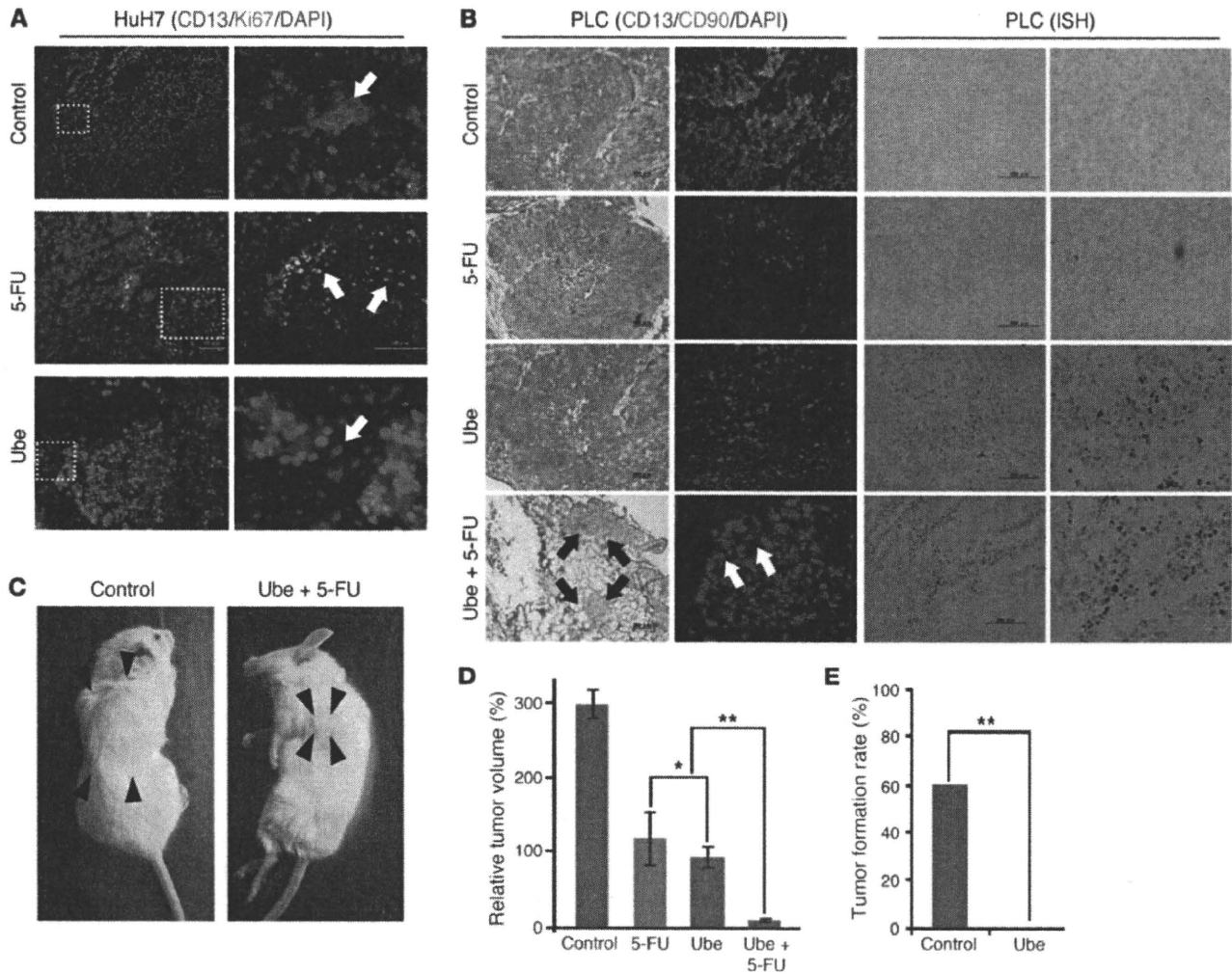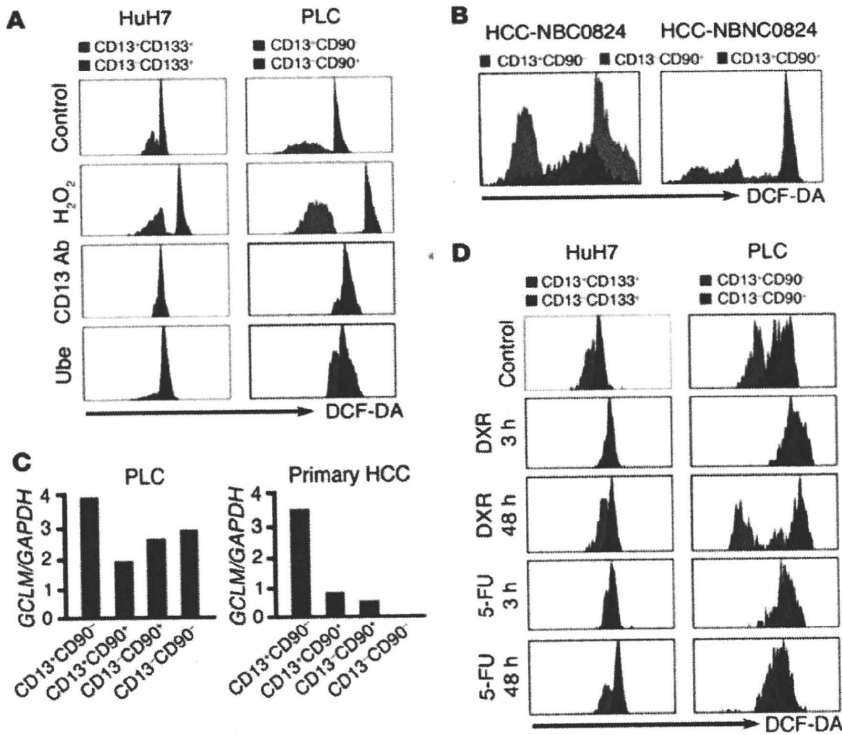
Figure 6
CD13 inhibition elicits cancer regression in vivo. (**A**) HuH7-xenografted mice were treated with 5-FU or ubenimex for 3 days. The sections were stained with anti-human CD13 (red), Ki-67 (green), and DAPI (blue). Each right-hand panel shows a high magnification (×20, control and 5-FU; ×40, Ube) of the white dot square on the left (×10, control and 5-FU; ×20, Ube). White arrows: cellular clusters express CD13 but not Ki-67 (upper panels), residual Ki-67+ cancer cells (middle panels), and a residual CD13+ cell (lower panels). (**B**) PLC/PRF/5-xenografted mice were treated with 5-FU, ubenimex, and ubenimex plus 5-FU for 14 days. The black arrows indicate a small amount of residual cancer. The sections were stained with H&E (×10), anti-human CD13 (red), anti-human CD90 (green), and DAPI (blue) (×20, control, 5-FU, and Ube; ×40, Ube + 5-FU). Nonspecific and fragmented expression of CD13 (white arrow). In situ hybridization for DNA fragmentation (low and high magnification). Black dot-like structures indicate labeled DNA. (**C**) Tumors of control and ubenimex–plus–5-FU–treated mice. Black arrowheads indicate the tumor margin. (**D**) The relative tumor volumes (after treatment [mm³]/before treatment [mm³] × 100%) of the control, 5-FU, ubenimex, and ubenimex–plus–5-FU–treated mice. Data represent mean ± SD from independent experiments. *NS; **$P < 0.01$. (**E**) The CD13+ cell–enriched fractions obtained from 5-FU–treated mice were serially transplanted into secondary NOD/SCID mice. The mice were treated with ubenimex (Ube; $n = 6$) or received no treatment (control; $n = 10$) from the day after transplantation for 7 days. Tumor growth was observed for 3 weeks.

most of the CD90+ cells were disrupted and tumors were replaced by a majority of CD13+ cells. After ubenimex treatment (20 mg/kg every day for 14 days), not only were many CD90+ cells present but CD13+ cells were also identified. Interestingly, in cases in which both ubenimex and 5-FU were administered, the majority of tumor cells were disrupted. We identified atypical, nonspecific CD13 expression in these cases (Figure 6B). Taken together with the findings that CD90+ cells produce CD13+ cells within 24 hours and that almost all of the CD13+ cells were disrupted by ubenimex plus 5-FU treatment, the CD13+ cells that appeared in the ubenimex treat-

ment groups may have been newly produced from residual CD90+ cells. Costaining of Ki67 and CD13 revealed that CD13+ cells were negative for the expression of Ki67 (Supplemental Figure 5).

The highly deformed nuclei observed in the ubenimex–plus–5-FU treatment specimens suggested that DNA fragments were present. The DNA fragmentation status was thus assessed by in situ hybridization with terminal deoxynucleotidyl transferase (TdT). There were a few DNA fragments in both the control and 5-FU–treated specimens, whereas there were many more in the ubenimex-treated specimens. Especially in the specimens treated

Figure 7
CD13+ cells contain lower levels of ROS than CD13- cells. **(A)** The expression of prooxidant DCF-DA in CD13+CD133+ and CD13-CD133+ HuH7 cells and CD13+CD90- and CD13-CD90+ PLC/PRF/5 cells. Controls, treated with 10 μg/ml of mouse anti-human IgG. As positive controls, cells were treated with 100 μM of oxidant H_2O_2 for 2 hours. Cells were treated with 5 μg/ml of CD13-neutralizing antibody and 25 μg/ml of ubenimex for 4 hours. **(B)** The expression of ROS in the CD13+CD90-, CD13-CD90+, and CD13+CD90+ fractions of 2 clinical HCC samples. **(C)** The expression of the ROS scavenger pathway gene *GCLM* in isolated CD13+CD90-, CD13+CD90+, CD13-CD90+, and CD13-CD90- cells from PLC/PRF/5 and clinical HCC samples estimated by semiquantitative RT-PCR. **(D)** The time-course change of ROS expression in DXR or 5-FU treatment. Cells were treated with 1 μg/ml of DXR and 1 μg/ml of 5-FU continuously. After 3 hours and 48 hours of treatment, ROS levels in each population were measured.

with ubenimex plus 5-FU, there were numerous DNA fragments in residual tumor cells (Figure 6B).

After 14 days of treatment, the tumor volume was significantly decreased in the ubenimex-plus-5-FU groups compared with the control and 5-FU or ubenimex groups (Figure 6, C and D).

Next, we studied the effects of CD13 inhibition as it pertains to the self-renewing ability of cells and repopulation of tumors. The CD13+-enriched fraction obtained from 5-FU–treated mice was serially transplanted into secondary NOD/SCID mice. Starting the day after transplantation, the mice were treated with ubenimex (20 mg/kg) for 7 days. After 3 weeks, no tumor formation was observed in the ubenimex-treated mice ($n = 0/6$), whereas 60% of the untreated mice grew tumors ($n = 6/10$) (Figure 6E).

The CD13+ HCC cells contain lower levels of ROS. We focused on the ROS scavenger pathway to determine why DNA fragmentation and apoptosis were induced by CD13 inhibition. It has been reported that self-renewing dormant stem cells normally possess low levels of intracellular ROS and that deregulation of ROS levels impairs stem cell functions (27). Intracellular ROS levels were measured by prooxidants using the 2′,7′-dichlorofluorescein diacetate (DCF-DA) stain. Both in HuH7 and PLC/PRF/5, the CD13+ fraction contained lower concentrations of ROS than the CD133strong and CD90+ fractions. After stimulation of oxidative stress by H_2O_2, a lower concentration of ROS was clearly observed in the CD13+ fraction compared with the CD13- fraction. Following treatment with the CD13-neutralizing antibody or ubenimex, the ROS concentration was significantly increased in CD13+ cells and reached the level of ROS observed in the CD13- fraction (Figure 7A). In clinical HCC samples, the results were similar to those in PLC/PRF/5, as the CD13+CD90- fraction exhibited lower ROS levels than those in the CD13-CD90+ and CD13+CD90+ fractions (Figure 7B). The CD13+ fraction also contained another ROS indica-

tor, MitoSOX (a highly selective marker for mitochondrial superoxide), which was markedly lower in the PLC and clinical HCC samples and less in HuH7 (Supplemental Figure 6).

To study the correlation between CD13 and the ROS scavenger pathway, the expression of *Gclm* was assessed by RT-PCR. *Gclm* encodes the glutamate-cysteine ligase that catalyses the rate-limiting synthesis step of glutathione (GSH), which works as a critical cellular reducing agent and anti-oxidant. *Gclm* was overexpressed in the CD13+CD90- fraction ($P < 0.001$) compared with the CD13+CD90+, CD13-CD90+, and CD13-CD90- fractions in PLC/PRF/5 and primary HCC cells (Figure 7C).

It is well known that cell destruction after exposure to cytotoxic chemotherapy and ionizing radiation is partially due to free radicals (28, 29). Given that the present study indicates a low ROS concentration in the CD13+ population, we were interested to see whether chemotherapy agents actually increase ROS level of CD13+ population. To study this, ROS levels of CD13+CD133+ and CD13-CD133+ populations in HuH7, and CD13+CD90- and CD13-CD90+ populations in PLC/PRF/5 were measured 3 hours and 48 hours after of DXR or 5-FU treatment. After 3 hours treatment with DXR, ROS levels were increased in both CD13+ and CD13- populations in HuH7 and PLC/PRF/5. Interestingly, after 48-hour treatment with DXR, ROS levels of CD13+ populations were decreased and reached those of control levels. Especially in PLC/PRF/5, CD13+CD90- populations showed 2 peaks of ROS levels, one of which contained further lowered ROS levels than control. With 5-FU treatment, though the power of upregulation of ROS levels was weaker than those of DXR, ROS levels of CD13+ fractions were actually increased to those of CD13- fractions. As with the data regarding DXR treatment, after 48 hours of 5-FU treatment, CD13+ populations showed lower levels of ROS compared with those of the CD13- population (Figure 7D). These data
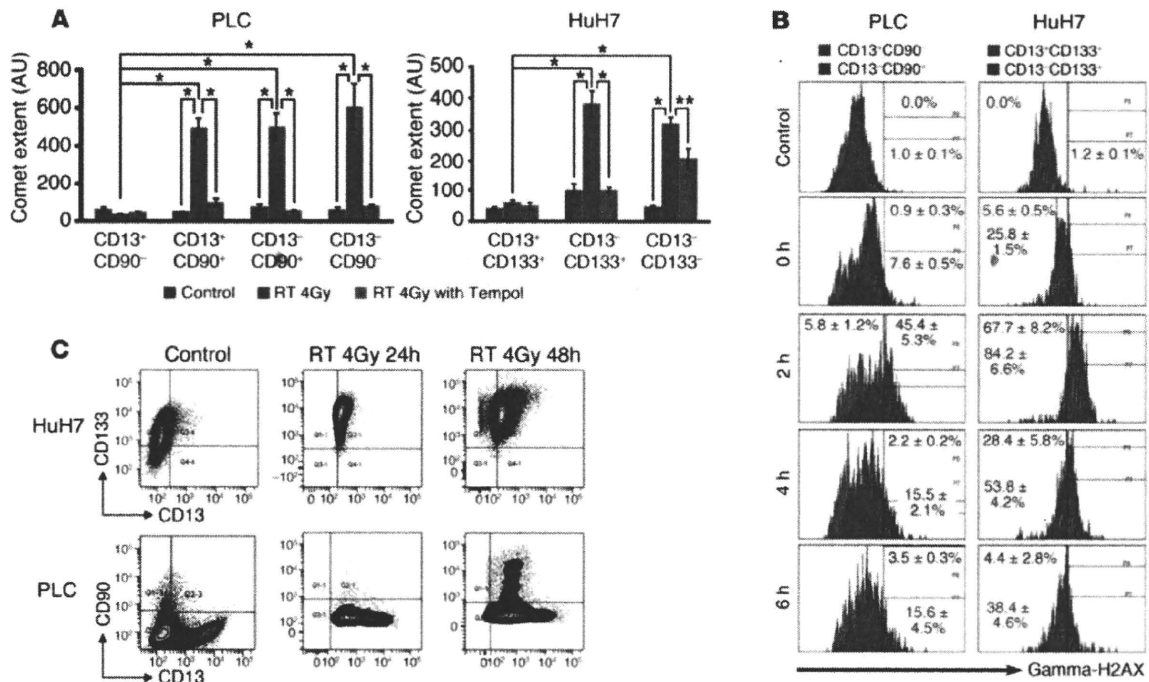
Figure 8
High levels of ROS scavenger expression parallel DNA damage in CD13+ HCC cells. (A) Isolated cell fractions of CD13+CD90-, CD13+CD90+, CD13-CD90+, and CD13-CD90- in PLC/PRF/5 and CD13+CD133+, CD13-CD133+, and CD13-CD133- in HuH7 were irradiated with 4 Gy with or without antioxidant tempol. Data show the tail lengths in the alkaline comet assay of control (blue), 4 Gy irradiation (brown), and antioxidant tempol pretreated (green) cells. *P < 0.01. **NS. (B) HuH7 and PLC/PRF/5 cells were irradiated with 4 Gy, and time course change of gamma-H2AX expression in each population was assessed. Numbers indicate the percentage of gamma-H2AX in CD13+CD90- PLC/PRF/5 and CD13+CD133+ HuH7 cells (red) and CD13-CD90+ PLC/PRF/5 and CD13-CD133+ HuH7 cells (blue) with ± SD. (C) HuH7 and PLC/PRF/5 cells were irradiated with 4 Gy, seeded in culture medium, and their expressions analyzed after 24 and 48 hours. Damaged and dead cells were eliminated with 7-AAD. The cut-off lines were determined using isotype controls.

together with the observation that CD13+ cells remained after treatment with chemotherapy agents (Figure 4A), suggest that ROS levels of all of the cells are temporally upregulated when cells are treated with chemotherapy agents and that this leads to disruption of the CD13 population, whereas in the CD13+ cells, ROS levels are downregulated by the ROS scavenger pathway and the cells survive. In addition, proliferative CD13 cells are easily affected by the DNA synthesis inhibition effect of chemotherapy agents.

To assess radiation-induced DNA damage with ROS, purified CD13+CD90-, CD13+CD90+, CD13-CD90-, and CD13-CD90- PLC/PRF/5 cells were irradiated and subjected to an alkaline comet assay. Although untreated cells did not show significantly different levels of DNA damage, there were fewer DNA strand breaks in CD13+CD90- cells than in the other 3 fractions (P < 0.01) after ionizing irradiation. The DNA damage in these 3 fractions (but not in the CD13+CD90- fraction) was significantly inhibited (P < 0.001) by treatment with an antioxidant reagent, tempol (Figure 8A). In HuH7 cells, the CD13- fraction also exhibited lower levels of DNA damage compared with the CD13- fraction. There was no significant difference between the irradiated and tempol-treated groups for the CD13-CD133- fraction (Figure 8A). These findings reveal that the enhanced ROS defenses in the CD13+ fraction contribute to the reduction in DNA damage after genotoxic cancer therapy. To confirm radiation-induced DNA double-strand break status in CD13+ and CD13 populations, time-course change of

gamma-H2AX, a marker of double-strand breaks (30), was studied. In PLC/PRF/5, after 4 Gy of irradiation, gamma-H2AX expression in CD13 CD90+ population increased after 2 hours of irradiation (45.4% ± 5.3%) and then decreased within 6 hours (15.6% ± 4.5%), whereas gamma-H2AX expression in CD13+CD90 population did not. In HuH7, gamma-H2AX expression increased after 2 hours in both CD13+CD133+ and CD13 CD133+ populations and decreased rapidly in the CD13+CD133+ population (4.4% ± 2.8%) compared with the CD13 CD133+ population (38.4% ± 4.6%) (Figure 8B). After 24 hours of irradiation, the residual cells were localized in the CD13+ fraction in HuH7 and in the CD13+CD90 fraction in PLC/PRF/5 (Figure 8C). Although there were some different manners in time-course change of gamma-H2AX in PLC/PRF/5 and HuH7, surviving cells after 24 hours of irradiation were localized in the CD13+ population, suggesting the radio-resistant characteristics of the CD13+ population, due to rapid recovery of DNA damage. After 48 hours of irradiation, the residual cells began to proliferate and produced CD13 CD133+ cells in HuH7 and CD13+CD90+ cells in PLC/PRF/5 (Figure 8C). These studies support the time-course studies (Figure 3C) and indicate that CD13+ cells exist as a core fraction in the cellular hierarchy.

Discussion
To achieve the goal of a radical cure for cancer, recurrence and metastasis caused by residual cancer cells are barriers that need to
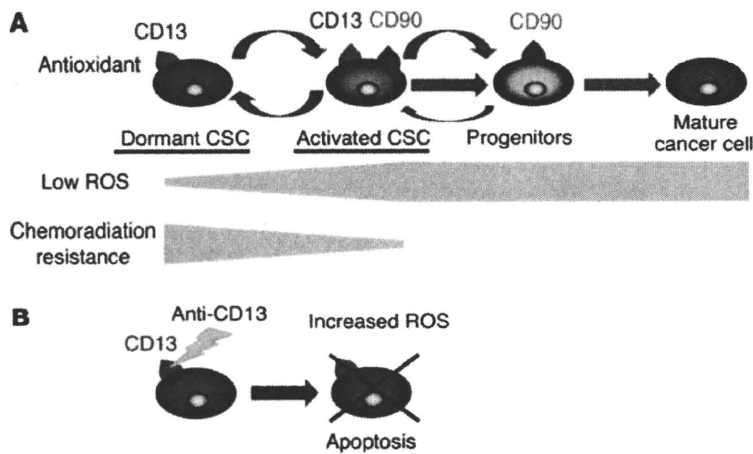
Figure 9
The CD13$^+$ CSCs of the liver generate genotoxic resistance through reduced levels of ROS (proposed schema). (**A**) Results indicate that CD13$^+$CD90$^-$ CSCs of the liver are dormant and exhibit reduced intracellular ROS levels and, because of increased antioxidants, may result in resistance to genotoxic chemo/radiation therapy. On the other hand, CD13$^-$CD90$^+$ CSCs actively proliferate and are sensitive to therapy. (**B**) Neutralization or inhibition of CD13 may result in an increase in intracellular ROS in CD13$^+$CD90$^-$ CSCs and induction of apoptosis.

be overcome. Recently, the presence of CSCs has attracted attention, and it is thought that these CSCs are intimately involved in cancer recurrence and resistance. In addition, as with leukemia (4, 5), the presence of dormant or slow-growing CSCs is beginning to be recognized in breast cancer (6). However, dormant or slow-growing CSCs have yet to be identified in most solid cancers. In the present study, we identified CD13 as a functional marker that can be used to identify potentially dormant liver CSCs resistant to treatment. Our exploration of SP cells has indicated that CD13$^+$ cancer cells are closely associated with SP cells. Cell-cycle studies indicated that CD13$^+$ cells exist in lower PY lesions. Cell-fate tracing assay with PKH26GL and immunohistochemical analysis of BrdU-retaining cells demonstrated that CD13$^+$ but not CD13$^-$ cells exhibited long dye retention and relatively slow proliferation in vitro and in vivo. This population possessed high tumorigenic potential in NOD/SCID mice and also induced chemo resistance. The results of this study are compatible with those of dormancy studies on hematopoietic stem/progenitor (3) and malignant cells (4, 5). CD13, also known as amino peptidase N, is a super family of zinc-binding metalloproteinases that play roles in cellular processes such as mitosis, invasion, cell adhesion, angiogenesis, radiation resistance, and antiapoptosis (31–34). To the best of our knowledge, there have been no reports describing the exclusive expression of CD13 in CSCs of the liver.

The immunohistochemical findings also support the view that CD13$^+$ cells play a role in relapse of liver cancer. The apparent increase in the number of CD13$^+$ cells near the fibrous capsule after TAE is consistent with the fact that clinical HCC relapse after TAE is frequent at the capsule site (7). These findings are compatible with the results of studies in mouse models that revealed that CD13$^+$ cells survived and were amplified after 5-FU treatment. In addition, the preferential accumulation of CD13$^+$ HCC cells at the capsule but not in the central region after TAE therapy suggests the attractive hypothesis that cellular components in the fibrous capsule may function as a protective niche (3).

The suppression of CD13 by the CD13-neutralizing antibody or ubenimex showed an effect even if the cancer cells were resistant to the ABC transporter–dependent agent DXR. This finding suggests that CD13$^+$ cells have some mechanism of resistance to anticancer agents in addition to their slow growth and ABC transporter (21, 35, 36) expressions. It is known that the control of ROS is indispensable for hematopoietic stem cell maintenance. Oxida-

tive stresses inhibit cellular dormancy and self renewal of hematopoietic stem cells (37, 38). In cancer, low ROS levels and radiation resistance in CD44$^+$CD24$^-$ breast CSCs has been reported (39). However, an association between ROS and self renewal in CSCs is unknown. In the present study, we demonstrated that CD13$^+$ cells contain low levels of ROS. The CD13$^-$CD133$^+$ and CD90$^+$ cells expressed higher levels of the ROS indicators DCF-DA and MitoSOX. RT-PCR of the ROS scavenger pathway gene *GCLM* and a comet assay also indicated that CD13$^+$ cells protect themselves from oxidant stress via the ROS pathway. Continuous treatment with anticancer agents predominantly elicits high levels of ROS in the CD13 population. However, in the CD13$^+$ population, it elicits low levels of ROS, and these cells survive and are enriched for after chemotherapy. Mice treated with ubenimex exhibited high DNA fragmentation in xenografted tumors. These findings suggest that the ROS scavenger pathway and CD13 are essential to CSC protection and maintenance in the liver (Figure 9, A and B). Importantly, tumorigenicity was completely inhibited by treatment with ubenimex in secondary mice xenografted with a CD13$^+$ cell–enriched tumor fraction obtained from 5-FU–treated mice. The suppression of CD13 inhibited self renewal and the tumor-initiation ability of CD13$^+$ cells. It is thought that deregulation of ROS pathway may contribute to disruption of CSCs.

The hierarchy analysis of PLC/PRF/5 cells revealed that a small fraction of CD90$^+$ cells produce a small number of CD13$^+$ cells in vitro. This finding indicates that activated CD90$^+$ cells should also be involved in targeted cancer therapy. The CD90$^+$ cells were resistant and remained in spite of treatment with ubenimex in vivo. The residual CD90$^+$ cells cause cancer regrowth and cancer recurrence by producing tumor-initiating CD13$^+$ cells. CD13$^+$ cells have high tumorigenicity and self-renewal ability in vivo. But unfortunately, in the case of liver cancer, it is difficult to target the proliferative CD90$^+$ cells by using conventional anticancer drugs because some parts of CD90$^+$ cells also express CD13. The expression of CD13 is closely related to the multidrug-resistant SP fraction, and CD13 protects cells from apoptosis via the ROS scavenger pathway. Of course, based on CSC concepts, tumors will disappear when CSCs are disrupted completely. This is because the loss of CSCs leads to the destruction of the hierarchical structure within the tumor. However, it may be difficult to obtain complete pharmacokinetic control, especially in vivo. Actually, in this study, we could not achieve complete disappearance of CD13$^+$ cells and

could not elicit tumor regression by single agent administration of ubenimex. To overcome these problems, we established combination therapy with ubenimex plus 5-FU to efficiently elicit tumor regression. Ubenimex works to disrupt CD13⁺ cells by its potential effect of upregulating ROS levels and its inhibition of self-renewal of CD13⁺ cells. 5-FU inhibits proliferative cancer cells, decreases tumor size, and improves survival. It is known that cell destruction after exposure to cytotoxic chemotherapy and ionizing radiation is partially due to free radicals (29, 39), and it is reported that 5-FU induces ROS in hematopoietic stem cells and suppresses the hematopoietic stem cell niche (40). We have also confirmed that 5-FU works to increase the ROS levels of CD13⁺ populations. By this combination therapy, tumors were drastically regressed compared with single-agent therapy. It is suggest that 5-FU and ubenimex work in a complementary or additive fashion.

Although the majority of the experiments in this study are based on cell lines, the expression, sphere, and ROS analyses support the contention that PLC/PRF/5 cells reflect clinical HCC and may hold promise for preclinical studies. This study also suggests that the future development of liver cancer therapy based on CSC concepts appears promising. We are attempting to establish human HCC-xenografted preclinical mouse models from clinical HCC samples to provide necessary confirmation of our contention using in vivo assays.

Methods

Cell culture. Human liver cancer cells, HuH7 and PLC/PRF/5, obtained from the Cell Resource Center for Biomedical Research, Institute of Development, Aging, and Cancer (Tohoku University, Sendai, Japan) were cultured in RPMI 1640 (Invitrogen) medium with 10% FBS (Equitech-Bio). Cells were cultured at 37°C in a humidified atmosphere containing 5% CO₂.

Flow cytometric analysis and cell sorting. The antibodies used in this study are listed in Supplemental Table 1. Briefly, cells were harvested with trypsin and EDTA. Doublet cells were eliminated using FSC-A/FSC-H and SSC-A/SSC-H. Dead and damaged cells were eliminated with 7-AAD (BD Biosciences – Pharmingen). Isotype controls (BD Biosciences) were used. FcR blocking was performed using an FcR-blocking reagent (Miltenyi-Biotec). FITC-conjugated anti-human CD45 (BD Biosciences – Pharmingen) and FITC-conjugated Lineage Cocktail (Lin1; BD Biosciences – Pharmingen), which contains antibodies against CD3, CD14, CD16, CD19, CD20, and CD56 and is used to detect lymphocytes, monocytes, eosinophils, and neutrophils, were used for eliminating hematopoietic cells in the clinical sample analysis. For sorting, cells were incubated with 1 μg of each antibody for 30 minutes. Control experiments involved incubation with each antibody for 30 minutes and no apparent increase in the number of dead cells detected by propidium iodide (PI) staining.

Cell-cycle assay. To characterize the SP fractions, 1 × 10⁶ cells in 2% FCS/1 mM HEPES buffer/DMEM were preincubated at 37°C for 30 minutes. Cells were then labeled with 10 μg/ml Hoechst 33342 (Molecular Probes) in staining medium at 37°C for 70 minutes. A total of 15 μg/ml reserpine (Sigma-Aldrich) was used for the Hoechst staining procedure. For cell-cycle analysis by PY staining, cells were first stained with Hoechst 33342 at 37°C. After 50 minutes, 1 μg/ml PY was added and the cells were incubated at 37°C for 20 minutes. FACSVantage SE DiVa (BD) and FACS SORP Aria (BD) were used for analysis and cell sorting. The cell cycle was also studied with 10 μg/ml 7-AAD (BD Biosciences – Pharmingen).

Gene expression study. Total RNA was prepared using TRIzoL reagent (Invitrogen). Reverse transcription was performed with SuperScriptIII (Invitrogen). Quantitative real-time RT-PCR was performed using a Light-Cycler TaqMan Master kit (Roche Diagnostics). The expression of mRNA

copies was normalized against *GAPDH* mRNA expression. The PCR primers used for amplification were as follows: *GCLM*, 5′-TGTGTGATGCCACCA-GATTT-3′ and 5′-TTCACAATGACCGAATACCG-3′; *GAPDH*, 5′-TTGGTATC-GTGGAAGGACTCA-3′ and 5′-TGTCATCATATTTG-GCAGGTTT-3′.

Cell proliferation and chemo-resistance assay. Isolated cells were seeded into 96-well culture plates at 5 × 10³ cells/well for cell proliferation assays. After 72 hours, cell viability was determined by an ATP bioluminescence assay (CellTiter-Glo Luminescent Cell Viability Assay; Promega) and the luminescence signal was detected using a luminometer (ARVO MX; Perkin-Elmer) according to the manufacturer's protocol. The cells were seeded onto 96-well culture plates at 5 × 10³ cells/well. After 24 hours, DXR was added to the culture medium (0.01, 0.05, and 0.1 μg/ml). After 72 hours of exposure to the chemotherapeutic agent, cell viability was determined using a method similar to that used in the cell proliferation assay.

Cell-fate tracing. Cells were labeled with 20 μM PKH26GL (Sigma-Aldrich) according to the manufacturer's protocol. Purified populations of cells were isolated and seeded onto 4-chamber polystyrene vessel tissue culture-treated glass slides (Falcon; BD Biosciences) at 5 × 10³ cells/well. Cells were cultured in RPMI 1640 (Invitrogen) medium with 20% FBS (Equitech-Bio). Cell fate was studied at each 30-minute time point for 238 hours using a time-lapse fluorescence microscope (BZ-9000 Biorevo; KEYENCE). Data were analyzed using a BZ-II analyzer (KEYENCE). BrdU-retaining cells were identified with fresh frozen samples with the modification of using 5-bromo-2′-deoxyuridine Labeling & Detection Kit 1 (Roche Applied Science) and CD13 rabbit polyclonal antibody (Santa Cruz Biotechnology Inc.). As secondary antibody, anti-rabbit IgG Alexa Fluor 555 (Molecular Probes) was used.

Sphere assay. Cells were seeded on ultra-low attachment culture dishes (Corning) in serum-free medium. DMEM/F-12 serum-free medium (Invitrogen) contained 2 mM L-glutamine, 1% sodium pyruvate (Invitrogen), 1% MEM nonessential amino acids (Invitrogen), 1% insulin-transferrin-selenium-X supplement (Invitrogen), 1 μM dexamethasone (Wako), 200 μM L-ascorbic acid 2-phosphate (Sigma-Aldrich), 10 mM nicotinamide (Wako), 100 μg/ml penicillin G, and 100 U/ml streptomycin supplemented with 20 ng/ml epithelial growth factor and 10 ng/ml fibroblast growth factor-2 (PeproTech). Digestion and cell passage were performed every 3 days.

Differentiation assays from spheres. Each single sphere established from normal liver cells was seeded into a culture chamber (BD Biosciences). Spheres were cultured in sphere medium containing 10% FBS to induce the differentiation process. Three days after the spheres became attached to the bottom of the chamber and spreading cells appeared, cells were fixed and stained with anti-human CD13 mouse monoclonal antibody (clone WM15, dilution 1:50; Santa Cruz Biotechnology Inc.), FITC–anti-human albumin goat polyclonal antibody (dilution 1:500; Bethyl Laboratories), anti-human Cytokeratin 19 mouse monoclonal antibody (clone RCK108, dilution 1:50; Dako), and anti-human α-fetoprotein mouse monoclonal antibody (clone 189502, concentration 5 μg/ml; R&D Systems).

Immunohistochemistry. The 4-μm-thick sections were obtained using cryostat and fixed with 4% paraformaldehyde for 15 minutes. After 1 hour of blocking, the sections were incubated overnight at 4°C in a humidified chamber with primary antibodies. For primary antibodies, anti-human CD13 mouse monoclonal antibodies (clone WM15, dilution 1:50; Santa Cruz Biotechnology Inc.), anti-human CA9 rabbit polyclonal antibodies (dilution 1:1000; Novus Biologicals), anti-human CD90 rabbit monoclonal antibodies (dilution 1:1000; Epitomics), and anti-human Ki-67 rabbit polyclonal antibodies (dilution 1:100; Santa Cruz Biotechnology Inc.) were used. For secondary antibodies, goat anti-mouse IgG₁, Alexa Fluor 546-conjugated, and highly cross-adsorbed (Molecular Probes) as well as goat anti-rabbit IgG, Alexa Fluor 488-conjugated and highly cross-adsorbed (Molecular Probes) antibodies were used. The coverslips were mounted using ProLong Gold and SlowFade Gold Antifade Reagent (Molecular

Probes), and the slides were viewed with a fluorescence microscope (BZ-9000 Biorevo). Data were analyzed using BZ-II (Keyence). The continuous cryostat sections were also stained with modified H&E.

Tumor cell preparation. Primary liver cancer samples were obtained from Osaka University with the patients' informed consent and the approval of the Research Ethics Board of Osaka University. Tumor tissues were cut into approximately 2-mm fragments, further minced with a sterile scalpel, and washed twice with DMEM/10% FBS. They were then placed in DMEM/10% FBS with 2 mg/ml collagenase A (Roche Diagnostics) solution. The mixture was incubated at 37°C with shaking until digestion was complete. Cells were filtered through a 40-μm nylon mesh and washed twice and the cell fragments and debris were then eliminated by Ficoll (GE Healthcare) density gradient centrifugation and stained for flow cytometry.

Inhibition of CD13. A total of 5×10^3 cells were seeded into 96-well plates in 200 μl of culture medium. After 24 hours, the medium was replaced with fresh culture medium containing 1, 5, 10, and 20 μg/ml mouse monoclonal anti-human CD13 antibodies (clone WM15; GeneTex) or 25, 50, 100, 250, and 500 μg/ml ubenimex (Nippon Kayaku). Cell viability was assayed at 24, 48, and 72 hours using Cell Counting Kit-8 (Dojindo) according to the manufacturer's instructions. Absorbance was measured at 450 nm using a 680 XR microplate reader (Bio-Rad). A total of 10 ng IgG_1 mouse monoclonal antibody (GeneTex) was used as the negative control. DXR-resistant (DXR-R) HuH7 cells were established by continuous treatment with 1 μg/ml DXR and selection of resistant colonies. Cellular apoptosis was measured using PI and APC-annexin V (BD Pharmingen) with an Apoptosis Detection Kit (BioVision).

In vivo assay. The xenografted mouse model was created by injection of 1×10^5 HuH7 and PLC/PRF/5 cells into NOD/SCID mice under anesthesia. For injection, the cells were resuspended in a 1:1 mixture of medium and Matrigel (BD Biosciences). The HuH7 cell-xenografted mice were treated with 5-FU (30 mg/kg; intraperitoneal administration) or ubenimex (20 mg/kg; oral administration) for 3 days. On the following day, mice were sacrificed and tumors were enucleated for the immunohistochemical assay. In the studies of PLC/PRF/5 cell-xenografted mice, mice were treated with 5-FU (30 mg/kg, 5 days of intraperitoneal injection and 2 days of withdrawal, 2 courses; 14 days), ubenimex (20 mg/kg, 14 days of forced oral administration), or ubenimex and 5-FU (combination of 2 courses of 30 mg/kg of 5-FU and 14 days of 20 mg/kg of ubenimex). The tumor size was calculated as follows: tumor volume $(mm^3) = a \times b/2$, where a = long axis and b = short axis. The relative tumor volume was calculated as follows: relative tumor volume (%) = $a/b \times 100$, where a = tumor volume before treatment (mm^3) and b = tumor volume after 14 days of treatment. The day after 14 days of treatment, mice were sacrificed and tumors were enucleated for immunohistochemical assay. The relative tumor volume was estimated as follows: relative tumor volume (mm^3) = tumor volume on the day after 14 days of treatment (mm^3)/tumor volume just before the start of treatment $(mm^3) \times 100$ (%). The residual tumors after 14 days of 5-FU treatment were enucleated and minced into 2-mm squares and subcutaneously transplanted into secondary NOD/SCID mice with Matrigel. The

mice were treated with ubenimex (20 mg/kg) from the day after transplantation for 7 days. Tumor growth was observed for 3 weeks. We used 4 or more mice for each model to enable statistical assessment of the results. All animal studies were approved by the Animal Experiments Committee at Osaka University.

ROS assay. To study intracellular ROS levels, cells were loaded with 10 μM of DCF-DA at 37°C for 30 minutes. ROS was activated by treatment with 100 μM H_2O_2 at 37°C for 120 minutes. To study the effect of CD13 inhibition on ROS levels, cells were pretreated with 5 μg/ml of the CD13-neutralizing antibody or 25 μg/ml of ubenimex at 37°C for 4 hours and stained with DCF-DA. For mitochondria ROS detection, cells were loaded with 5 μM MitoSOX (Molecular Probes) at 37°C for 20 minutes.

DNA fragmentation assay. For the alkaline comet assay, 5,000 isolated cells were irradiated (4 Gy) on ice and suspended in 0.6% of low melting point agarose, spread over the wells of slides, and immersed in alkaline solution for 30 minutes using a kit (Trevigen). Alkaline electrophoresis was then performed. Slides were stained with silver for visualization. For the tempol experiments, cells were treated with 10 mM of tempol (Sigma-Aldrich) for 15 minutes before irradiation. For in situ hybridization detection of fragmented DNA, 10-μm-thick serial sections obtained from fresh frozen samples were hybridized with TdT using tumor TACS in situ apoptosis detection kit (Trevigen) according to the manufacturer's protocols.

To identify DNA double-strand breaks, Alexa Fluor 488 Mouse Anti-H2AX (BD Pharmingen) was used according to the manufacturer's protocols. Briefly, cells were irradiated at 4 Gy. Cells were incubated in culture medium at 37°C in a humidified atmosphere containing 5% CO_2 after irradiation for 0, 2, 4, and 6 hours. After incubation, cells were stained with cell-surface antibodies. Then cells were fixed and permeabilized using Cytofix/Cytoperm Fixation/Permeabilization Solution Kit (BD), and stained with Alexa Fluor 488 Mouse Anti-H2AX.

Statistics. We determined statistical significance by 1-tailed Student's t test. $P < 0.05$ was defined as significant.

Address correspondence to: Masaki Mori, Department of Gastroenterological Surgery, Graduate School of Medicine, Osaka University, 2-2 Yamadaoka, Suita 565-0871, Japan. Phone: 81.6.6879.3251; Fax: 81.6.6879.3259; E-mail: mmori@gesurg.med.osaka-u.ac.jp.

1. Visvader JE, Lindeman GJ. Cancer stem cells in solid tumours: accumulating evidence and unresolved questions. *Nat Rev Cancer.* 2008;8(10):755–768.
2. Lapidot T, et al. A cell initiating human acute myeloid leukaemia after transplantation into SCID mice. *Nature.* 1994;367(6464):645–648.
3. Arai F, et al. Tie2/angiopoietin-1 signaling regulates hematopoietic stem cell quiescence in the bone marrow niche. *Cell.* 2004;118(2):149–161.
4. Guan Y, Gerhard B, Hogge DE. Detection, isolation, and stimulation of quiescent primitive leukemic progenitor cells from patients with acute myeloid leukemia (AML). *Blood.* 2003;101(8):3142–3149.
5. Holyoake T, Jiang X, Eaves C, Eaves A. Isolation of a highly quiescent subpopulation of primitive leukemic cells in chronic myeloid leukemia. *Blood.* 1999; 94(6):2056–2064.
6. Meng S, et al. Circulating tumor cells in patients with breast cancer dormancy. *Clin Cancer Res.* 2004; 10(24):8152–8162.
7. El-Serag HB, Rudolph KL. Hepatocellular carcinoma: epidemiology and molecular carcinogenesis. *Gastroenterology.* 2007;132(7):2557–2576.
8. Haraguchi N, et al. Characterization of a side population of cancer cells from human gastrointestinal system. *Stem Cells.* 2006;24(3):506–513.
9. Ma S, et al. Identification and characterization of tumorigenic liver cancer stem/progenitor cells. *Gastroenterology.* 2007;132(7):2542–2556.
10. Ding W, et al. CD133+ liver cancer stem cells from methionine adenosyl transferase 1A-deficient mice demonstrate resistance to transforming growth factor (TGF)-beta-induced apoptosis. *Hepatology.* 2009; 49(4):1277–1286.
11. Zhu Z, et al. Cancer stem/progenitor cells are highly enriched in CD133(+)CD44(+) population in hepatocellular carcinoma. *Int J Cancer.* 2009; 126(9):2067–2078.
12. Yang ZF, et al. Significance of CD90+ cancer stem

cells in human liver cancer. *Cancer Cell.* 2008; 13(2):153–166.

13. Yang ZF, et al. Identification of local and circulating cancer stem cells in human liver cancer. *Hepatology.* 2008;47(3):919–928.

14. Yamashita T, et al. EpCAM-positive hepatocellular carcinoma cells are tumor-initiating cells with stem/progenitor cell features. *Gastroenterology.* 2009;136(3):1012–1024.

15. Ashmun RA, Shapiro LH, Look AT. Deletion of the zinc-binding motif of CD13/aminopeptidase N molecules results in loss of epitopes that mediate binding of inhibitory antibodies. *Blood.* 1992; 79(12):3344–3349.

16. Look AT, Ashmun RA, Shapiro LH, Peiper SC. Human myeloid plasma membrane glycoprotein CD13 (gp150) is identical to aminopeptidase N. *J Clin Invest.* 1989;83(4):1299–1307.

17. Ashmun RA, Look AT. Metalloprotease activity of CD13/aminopeptidase N on the surface of human myeloid cells. *Blood.* 1990;75(2):462–469.

18. Nakamura H, Suda H, Takita T, Aoyagi T, Umezawa H. X-ray structure determination of (2S, 3R)-3-amino-2-hydroxy-4-phenylbutanoic acid, a new amino acid component of bestatin. *J Antibiot.* 1976; 29(1):102–103.

19. Mathé G. Bestatin, an aminopeptidase inhibitor with a multi-pharmacological function. *Biomed Pharmacother.* 1991;45(2–3):49–54.

20. Kobayashi T, et al. Randomized trials between behenoyl cytarabine and cytarabine in combination induction and consolidation therapy, and with or without ubenimex after maintenance/intensification therapy in adult acute myeloid leukemia. The Japan Leukemia Study Group. *J Clin Oncol.* 1996; 14(1):204–213.

21. Hadnagy A, Gaboury L, Beaulieu R, Balicki D. SP analysis may be used to identify cancer stem cell populations. *Exp Cell Res.* 2006;312(19):3701–3710.

22. Vander Borght S, et al. Expression of multidrug resistance-associated protein 1 in hepatocellular carcinoma is associated with a more aggressive tumour phenotype and may reflect a progenitor cell origin. *Liver Int.* 2008;28(10):1370–1380.

23. Kamiya A, Kakinuma S, Yamazaki Y, Nakauchi H. Enrichment and clonal culture of progenitor cells during mouse postnatal liver development in mice. *Gastroenterology.* 2009;137(3):1114–1126.

24. Kaluz S, Kaluzová M, Liao SY, Lerman M, Stanbridge EJ. Transcriptional control of the tumor- and hypoxia-marker carbonic anhydrase 9: A one transcription factor (HIF-1) show? *Biochim Biophys Acta.* 2009;1795(2):162–172.

25. Miyamoto K, et al. Foxo3a is essential for maintenance of the hematopoietic stem cell pool. *Cell Stem Cell.* 2007;1(1):101–112.

26. Moore KA, Lemischka IR. Stem cells and their niches. *Science.* 2006;311(5769):1880–1885.

27. Naka K, Muraguchi T, Hoshii T, Hirao A. Regulation of reactive oxygen species and genomic stability in hematopoietic stem cells. *Antioxid Redox Signal.* 2008;10(11):1883–1894.

28. Estrela JM, Ortega A, Obrador E. Glutathione in cancer biology and therapy. *Crit Rev Clin Lab Sci.* 2006; 43(2):143–181.

29. Riley P. Free radicals in biology: oxidative stress and the effects of ionizing radiation. *Int J Radiat Biol.* 1994; 65(1):27–33.

30. Chen HT, et al. Response to RAG-mediated VDJ cleavage by NBS1 and gamma-H2AX. *Science.* 2000; 290(5498):1962–1965.

31. Hashida H, et al. Aminopeptidase N is involved in

cell motility and angiogenesis: its clinical significance in human colon cancer. *Gastroenterology.* 2002; 122(2):376–386.

32. Menrad A, Speicher D, Wacker J, Herlyn M. Biochemical and functional characterization of aminopeptidase N expressed by human melanoma cells. *Cancer Res.* 1993;53(6):1450–1455.

33. Mishima Y, et al. Leukemic cell-surface CD13/ aminopeptidase N and resistance to apoptosis mediated by endothelial cells. *J Natl Cancer Inst.* 2002;94(13):1020–1028.

34. Petrovic N, et al. CD13/APN regulates endothelial invasion and filopodia formation. *Blood.* 2007; 110(1):142–150.

35. Aihara M, et al. A combined approach for purging multidrug-resistant leukemic cell lines in bone marrow using a monoclonal antibody and chemotherapy. *Blood.* 1991;77(9):2079–2084.

36. Fairchild CR, et al. Carcinogen-induced mdr overexpression is associated with xenobiotic resistance in rat preneoplastic liver nodules and hepatocellular carcinomas. *Proc Natl Acad Sci U S A.* 1987; 84(21):7701–7705.

37. Ito K, et al. Regulation of oxidative stress by ATM is required for self-renewal of haematopoietic stem cells. *Nature.* 2004;431(7011):997–1002.

38. Ito K, et al. Reactive oxygen species act through p38 MAPK to limit the lifespan of hematopoietic stem cells. *Nat Med.* 2006;12(4):446–451.

39. Diehn M, et al. Association of reactive oxygen species levels and radioresistance in cancer stem cells. *Nature.* 2009;458(7239):780–783.

40. Hosokawa K, et al. Function of oxidative stress in the regulation of hematopoietic stem cell-niche interaction. *Biochem Biophys Res Commun.* 2007; 363(3):578–583.